minerals

MDPI

Article

Stable Abiotic Production of Ammonia from Nitrate in Komatiite-Hosted Hydrothermal Systems in the Hadean and Archean Oceans

Manabu Nishizawa [1,2,*,†], Takuya Saito [1,2,†], Akiko Makabe [1,2,†], Hisahiro Ueda [1], Masafumi Saitoh [3,4], Takazo Shibuya [1,2,3,4] and Ken Takai [1,2,3,4]

1 Institute for Extra-Cutting-Edge Science and Technology Avant-Garde Research (X-Star), Super-Cutting-Edge Grand and Advanced Research (SUGAR) Program, Japan Agency for Marine-Earth Science and Technology (JAMSTEC), Yokosuka 237-0061, Japan; sai-tak@jamstec.go.jp (T.S.); makabea@jamstec.go.jp (A.M.); uedah@jamstec.go.jp (H.U.); takazos@jamstec.go.jp (T.S.); kent@jamstec.go.jp (K.T.)
2 Department of Subsurface Geobiological Analysis and Research (D-SUGAR), JAMSTEC, Yokosuka 237-0061, Japan
3 Research and Development (R&D) Center for Submarine Resources, JAMSTEC, Yokosuka 237-0061, Japan; saitoh.m.ab@gmail.com
4 Project Team for Development of New-Generation Research Protocol for Submarine Resources, JAMSTEC, Yokosuka 237-0061, Japan
* Correspondence: m_nishizawa@jamstec.go.jp
† These authors contributed equally to this work.

Abstract: Abiotic fixation of atmospheric dinitrogen to ammonia is important in prebiotic chemistry and biological evolution in the Hadean and Archean oceans. Though it is widely accepted that nitrate (NO_3^-) was generated in the early atmospheres, the stable pathways of ammonia production from nitrate deposited in the early oceans remain unknown. This paper reports results of the first experiments simulating high-temperature, high-pressure reactions between nitrate and komatiite to find probable chemical pathways to deliver ammonia to the vent–ocean interface of komatiite-hosted hydrothermal systems and the global ocean on geological timescales. The fluid chemistry and mineralogy of the komatiite–H_2O–NO_3^- system show iron-mediated production of ammonia from nitrate with yields of 10% at 250 °C and 350 °C, 500 bars. The komatiite–H_2O–NO_3^- system also generated H_2-rich and alkaline fluids, well-known prerequisites for prebiotic and primordial metabolisms, at lower temperatures than the komatiite–H_2O–CO_2 system. We estimate the ammonia flux from the komatiite-hosted systems to be 10^5–10^{10} mol/y in the early oceans. If the nitrate concentration in the early oceans was greater than 10 µmol/kg, the long-term production of ammonia through thermochemical nitrate reduction for the first billion years might have allowed the subsequent development of an early biosphere in the global surface ocean. Our results imply that komatiite-hosted systems might have impacted not only H_2-based chemosynthetic ecosystems at the vent-ocean interface but also photosynthetic ecosystems on the early Earth.

Keywords: Hadean; abiotic nitrogen cycle; habitability; nitrate reduction; serpentinization

Citation: Nishizawa, M.; Saito, T.; Makabe, A.; Ueda, H.; Saitoh, M.; Shibuya, T.; Takai, K. Stable Abiotic Production of Ammonia from Nitrate in Komatiite-Hosted Hydrothermal Systems in the Hadean and Archean Oceans. *Minerals* **2021**, *11*, 321. https://doi.org/10.3390/min11030321

Academic Editors: Yasuhito Sekine, Elizabeth B. Rampe, Keisuke Fukushi and Edward J. O'Loughlin

Received: 8 February 2021
Accepted: 16 March 2021
Published: 19 March 2021

1. Introduction

The reduction of abundant dinitrogen (N_2) to ammonia (NH_3) is important for prebiotic chemical evolution and the early development of life on Earth. Ammonia participates in the synthesis of nitrogen-bearing organic compounds that are essential for cellular functions and self-reproduction (e.g., amino acids and nucleotides). Thus, the production of ammonia is assumed to be a prerequisite for origin-of-life scenarios, e.g., [1,2], and the development of microbial ecosystems in the Hadean and Archean oceans, e.g., [3–5]. Theoretical and observational assessments indicate that the main components of the early

atmosphere are N_2 and CO_2, e.g., [6–11]. Thus, high energy reactions are required to reduce chemically stable N_2. Previous studies have suggested that nitric oxide (NO) was produced by electrical discharges in the early atmosphere [3,12]. The resulting NO was likely converted into nitric acid (HNO_3) or nitrous acid (HNO_2) due to photochemical and aqueous-phase reactions, and it was eventually deposited in the ocean through rain [13]. This suggests ammonia was produced by the abiotic reduction of nitrate (NO_3^-) and nitrite (NO_2^-) in the early oceans because the oldest traces of early life were reported from 3.9–3.8 Ga sedimentary rocks of marine origin, e.g., [14–20], c.f. [21–23].

Iron-bearing materials are potential reductants for ammonia production from nitrate and nitrite in the early anoxic ocean. Accordingly, chemical reactions of nitrate and nitrite in the water column or marine sediments have been tested experimentally using ferrous ions and sulfate green rust ($Fe^{II}_4Fe^{III}_2(OH)_{12}SO_4 \cdot yH_2O$) at around 25 °C [24–27]. These experiments have provided the following three findings. (1) At 22 °C, Nitrite reduction by ferrous ions produces ammonia at pH $\geq$ 7.5, but ammonia production is suppressed in CO_2-saturated water with respect to $FeCO_3$. (2) Nitrate reduction by ferrous ions produces ammonia at pH > 8 in the presence of Cu^{2+}. (3) Sulfate green rust reduces nitrite and nitrate to ammonia at pH 7–8.3. These findings suggest that the reduction of nitrite and nitrate at around 25 °C depends highly on the composition of the aqueous solution and hardly occurs at acidic pH. Because the early oceans are thought to be CO_2-rich and sulfate-poor, with an acidic to slightly alkaline pH (ca. 5.5–7.5) [8,9,11,28–30], the reduction of nitrite and nitrate may have been inhibited in the water column or marine sediments in these oceans at around 25 °C.

Seafloor hydrothermal environments are another potential site of pre-biotic ammonia production. Abiotic reduction of nitrate and nitrite has been examined under simulated hydrothermal conditions with transition metal sulfides ($Fe_{1-x}S$, FeS_2, NiS, Cu_2S, $CuFeS_2$), oxides (Fe_3O_4, NiO, Cu_2O), and iron-nickel alloys [31–34]. The results of these experiments have shown that some minerals participate in the reduction of nitrate and/or nitrite to ammonia, while others participate in the reduction of nitrate and/or nitrite to other forms of nitrogen (putatively N_2 or N_2O). Major anions (e.g., chloride, phosphate, sulfate, and dissolved carbonate species) further suppress nitrate reduction by $Fe_{1-x}S$ at room temperature due to competing adsorption onto $Fe_{1-x}S$ [31]. Given that concentrations of transition metal sulfides are typically found in hydrothermal mounds where high-temperature fluids mix with cold seawater, the reactions examined in previous studies [31–34] occur in nature under fluctuations and steep gradients of temperature, pH, and redox potential. These fluctuations and the associated unstable environment in hydrothermal mounds should result in a lower conversion to ammonia than in the laboratory experiments, with the exception of the relatively robust reduction of nitrite to ammonia catalyzed by MoS with geoelectrical current [35]. These results imply that other mechanisms for the sustainable supply of ammonia to the early oceans are favorable both for the pre-biotic chemical evolution in hydrothermal vent environments and the accumulation of ammonia in the global ocean.

This study focused on the reaction of nitrate with oceanic crust under high temperature and high-pressure conditions. Such reactions probably occur in the recharge and reaction zones of hydrothermal systems (i.e., sub-seafloor environments) and have affected the composition of vent fluids and the budget of nitrogen species in the early oceans. At present, the ammonia concentration in high-temperature hydrothermal fluids in sediment-free systems is typically similar to that of ambient deep-sea water (1 μm or less), although occasionally it is as high as 15 μm at certain locations [36,37]. These observations suggest the possibility of abiotic reduction of nitrate in seawater (40 μm) within oceanic crust. However, the simultaneous complex processing of nitrogen compounds by thermophilic microorganisms within hot oceanic crusts can obscure the signal of abiotic nitrate chemistry, as observed for nitrogen dynamics in geothermal environments [38]. Thus, an experimental approach is required to understand the abiotic chemistry of nitrate within hot oceanic crusts and the resultant vent fluid composition.

This paper reports the first experimental results of a simulation of high-temperature, high-pressure reactions between nitrate and komatiite to find chemical pathways that may have delivered ammonia to the vent–ocean interface and the global ocean on geological timescales. Komatiite is an ultramafic lava (MgO > 18%) produced by exceptionally hot melting in mantle upwellings, e.g., [39]. Most komatiite eruptions occurred between 3.5 and 1.5 Ga [40], and komatiite is believed to be the predominant ultramafic rock on the Hadean–Archean seafloor. The young Earth was hotter, and a thick layer of oceanic crust (more than three times greater than the present-day equivalents) probably restricted the eruption of mantle peridotites to the seafloor [41,42]. Therefore, rather than peridotite-hosted hydrothermal systems at slow-spreading mid-oceanic ridges, komatiite-hosted hydrothermal systems on oceanic islands and/or plateaus has been hypothesized to generate H_2-rich and alkaline fluids [43], which are prerequisites for pre-biotic and primordial metabolisms at the vent–ocean interface, e.g., [43–46]. On the basis of the findings of the present study, the roles of komatiite-hosted hydrothermal systems on pre-biotic chemistry and implications for biological nitrogen metabolism and the global nitrogen cycle on the early Earth were explored.

2. Materials and Methods

Synthesis of komatiite, hydrothermal reaction experiments and chemical/mineralogical analyses of the reactants and products were conducted at Japan Agency for Marine-Earth Science and Technology (JAMSTEC). Details were provided in previous publications [47–52].

2.1. Starting Materials

Komatiite used in the experiments was synthesized from a mixture of 12 reagents (i.e., SiO_2, TiO_2, Al_2O_3, Fe_2O_3, MnO, MgO, $CaCO_3$, Na_2CO_3, K_2CO_3, P_2O_5, NiO, and Cr_2O_3) by stepwise heating and cooling at oxygen fugacity of the quartz–fayalite–magnetite buffer. Mixing ratios of the reagents were adjusted to make Al-depleted (Barberton-type) komatiite more representative of ultramafic volcanism in Hadean oceanic islands and/or plateaus with a hotter mantle upwelling (plume) compared with Al-undepleted (Munro-type) komatiite [49]. The synthetic komatiite was primarily composed of olivine and glass. The komatiite was crushed using a tungsten mortar and an agate mill and then sieved to obtain particles smaller than 90 μm. Approximately 30 g of the powdered komatiite was ultrasonically washed with acetone and pure water (18.4 MΩ cm at 25 °C) several times and freeze-dried in a vacuum to remove possible contamination by organic matter during sample preparation. Specifically, carbon and nitrogen contents of the resultant komatiite sample were 210 ppm and 0.5 ppm, respectively [52].

Simulated aqueous solutions of Hadean seawater containing nitrate were prepared with the following compositions: 1000 mmol/kg NaCl and 10 mmol/kg $NaNO_3$ for the experiment at 250 °C; and 1000 mmol/kg NaCl and 0.94 mmol/kg KNO_3 for the experiment at 350 °C. Prior to use, the NaCl reagent was baked at 450 °C for 5 h under atmosphere to combust any organic contaminants.

We also conducted hydrothermal experiments without komatiite to test nitrate reduction in the H_2O–NO_3^- system at 250 °C and 350 °C under 500 bars (experiments N250C and N350C). The initial aqueous solutions were prepared with the following composition: 1000 mmol/kg NaCl and 10 mmol/kg KNO_3.

2.2. Hydrothermal Experiments

The hydrothermal reaction experiments were conducted in a flexible-cell hydrothermal apparatus consisting of a flexible gold bag with a titanium head (reaction cell) enclosed in an Inconel® alloy autoclave (modified after [53]). Prior to the experiments, the titanium head attached to the gold bag was completely oxidized to TiO_2 to eliminate possible H_2 generation by a reaction between metallic titanium and water at the experimental conditions. All materials in contact with the reacting fluid (i.e., gold bag, titanium head,

and gold-lined sampling tube) were baked at 450 °C for 5 h under atmosphere in a muffle furnace to remove any organic contamination.

Approximately 10–12 g of the komatiite powder was initially reacted with 64–72 g of the simulated Hadean seawater in the reaction cell at 250 °C and 350 °C, under 500 bars (experiments N250 and N350). Changes in fluid composition were monitored by collecting 3–5 g of fluid samples multiple times during the ongoing experiment from the reaction cell through the gold-lined sampling tube while maintaining the temperature at 250 °C or 350 °C and the pressure at 500 bars. Consequently, the water–rock mass ratios decreased from 7 to 4 during experiment N250 (4870 h) and from 5 to 3 during experiment N350 (2515 h). These experimental conditions mimic the high-temperature regions in sub-seafloor hydrothermal systems where the water–rock mass ratios are generally below 5 [54]. After the experiments, solid reaction products were freeze-dried in a vacuum and then stored in a vacuum desiccator until mineral compositions could be analyzed.

2.3. Chemical and Mineralogical Analyses

2.3.1. Aqueous Fluids

For pH analysis, 1.0 mL of fluid was collected in a vial and the pH was measured by a pH meter (LAQUAtwin; HORIBA Ltd., Kyoto, Japan) at a room temperature under atmospheric conditions. The estimated precision of pH measurement was ±0.2 units of the reported value. For H_2 analysis, 0.5 mL of fluid was introduced to an Ar-purged vial. The vial was left for 30 min to be reached in equilibrium at a room temperature. The H_2 and N_2O concentrations in the headspace of the vial was measured by gas chromatography with dielectric- barrier discharge ionization detector (GC-BID) (Nexis GC-2030, SHIMADZU Corp., Kyoto, Japan). The analytical precision (1SD) of replicate measurements was typically better than 5% for H_2 and N_2O at 100 ppm.

For cation analyses, 0.2 mL of fluid was sampled in a vial and diluted with 10 mL of pure water. The final pH of the diluted solution was adjusted to 2 by adding 0.2 mL of 1N HNO_3 to avoid mineral precipitation. For anion analyses, 0.2 mL of fluid was collected and diluted with 10 mL of pure water. The final pH of the diluted solution was adjusted to 12 by adding 0.2 mL of 1N NaOH was added to avoid the precipitation of amorphous silica. The concentrations of Cl, and Na were analyzed by ion chromatography (Dionex ICS-1600/2100; Thermo Fisher Scientific, Waltham, MA, USA), while those of K, Ca, Mg, Fe, Mn, and Si were analyzed by inductively coupled plasma optical emission spectrometry (ICP-OES) (Spectro ARCOS; AMETEK, Berwyn, PA, USA). The analytical precision (1SD) of replicate measurements was typically better than 2% for Cl, Na, and K, and typically better than 5–10% for the other elements depending on their concentrations.

The nitrate and nitrite concentrations were measured using ion chromatography (IC-Pac A25S column; Thermo Fisher Scientific, Waltham, MA, USA) with UV detection at 220 nm (GL-7451; GL Science, Tokyo, Japan) (the detection limit was 0.1 μmol/kg and the reproducibility was better than 3%) [51]. The ammonium concentration in the reacted fluid was determined with fluorescence photometry after reacting at 50 °C with a 20 mmol/kg orthophthaldialdehyde solution and a 200 mmol/kg sodium borate solution containing 2 mmol/kg of sodium sulfite [52]. The analytical precision (1SD) of replicate measurements was typically better than 1%, 4%, and 3% for nitrate, nitrite and ammonium, respectively.

2.3.2. Solids

Initial characterization of the morphology and chemical composition of the solid reaction products was performed after the experiments using scanning electron microscopes (SEM) equipped with energy dispersive X-ray spectrometers (EDX) (a Hitachi High-Tech Miniscope® TM3000 and a FEI Quanta 450 FEG). Data on the mineral assemblages of reaction products were obtained by X-ray diffraction (XRD) and Raman spectroscopy using a Rigaku MiniFlex II and a Nanophoton RAMANtouch. Quantitative compositional data of the reaction products were obtained through electron probe micro analysis (EPMA) with wavelength dispersive X-ray spectroscopy using a JEOL JXA–8500F. The whole-rock

compositions of 10 major elements (i.e., Si, Ti, Al, Fe, Mn, Mg, Ca, Na, K, and P) of the synthetic komatiite were analyzed by X-ray Fluorescence (XRF) using a Rigaku ZSX Primus II. Three types of samples were prepared from the solid reaction products for the morphological, mineralogical and compositional analyses. The first group comprises fragments mounted in epoxy resin and polished by silicon carbide powder and diamond paste to determine the cross sections of the solid products. Samples in the second group were crushed using a stainless spatula, and the resulting sub-millimeter size grains were mounted on a glass slide with carbon tape or double-sided tape to examine 3D structures. Half of the second group samples were washed further with ethanol and purified water in an ultrasonic cleaner to remove the suspended fraction. The procedure was repeated until the ethanol and water were no longer cloudy. The washed samples were dried in a vacuum at 40 °C and then mounted on a glass slide. After examination using optical microscope and by Raman spectroscopy, the polished and crushed samples were coated with osmium or carbon particles for the analyses by SEM/EDX or EPMA, respectively. The third group of fragment samples was ground with agar mortar for XRD and XRF analyses. The resulting powder samples were processed further for XRF analysis to prepare glass beads using $Li_2B_4O_7$ reagent.

2.3.3. Thermodynamic Calculation

The $pH_{in\text{-}situ}$ of the sampled fluids was calculated using the Geochemists' Workbench computer code [55], based on pH at room temperature and the concentrations of dissolved species. Saturation index (SI) was calculated from the relation SI = log(Q/K), where Q is the activity quotient of the species involved in the reaction and K is the equilibrium constant. The required thermodynamic database was generated using the SUPCRT92 computer program [56] with thermodynamic data for aqueous species and complexes obtained from [57–60]. The B-dot activity model was used in the calculation of sampled fluids [61,62], and the activity coefficients of neutral species were assumed to be unity.

3. Results

3.1. Fluid Chemistry

Table 1 and Figure 1 present the concentrations of selected species measured for aqueous fluids in the komatiite–H_2O–NO_3^- system as a function of time at 250 °C and 350 °C under 500 bars. The pH values of the initial solutions of experiments N250 and N350 after the pressurization to 500 bars at room temperature were approximately 9. During the high temperature water-rock reactions, the pH measured at room temperature ($pH_{25°C}$) decreased from the initial values of 9.6 and 7.2 to the steady-state values of 8.6 (alkaline) and 5.7 (acidic) at 250 °C and 350 °C, respectively. "Steady state" here refers to the condition under which the concentration of a given dissolved species changes little with time [49,50]. The concentrations of almost all major species in the experiments (with the exception of H_2 and Ca) reached a steady state within 300 h at both 250 °C and 300 °C.

The calculated in situ pH ($pH_{in\text{-}situ}$) decreased from 7.7 and 7.1 to the steady-state values of 5.6 and 5.0 at 250 °C and 350 °C, respectively. As neutral pH values at the experimental conditions are 5.46 at 250 °C and 5.56 at 350 °C, the komatiite–H_2O–NO_3^- system generated near neutral and acidic fluids at 250 °C and 350 °C, respectively.

The concentration of Cl remained relatively constant throughout the experiments because chlorine-containing minerals were rare in the altered komatiites. In contrast, the concentration of other species changed as the fluid/rock reactions progressed. Na concentrations steadily decreased by 30–40 mmol/kg from 990–1000 mmol/kg both at 250 °C and 350 °C, whereas K concentrations steadily increased by 1.5 and 1.1 mmol/kg from 0.3 and 1.0 mmol/kg at 250 °C and 350 °C, respectively. Ca and Si concentrations reached their maximum values and then decreased to the steady-state values (Si: 0.7 mmol/kg at 250 °C and 2.8 mmol/kg at 350 °C; Ca: 30 mmol/kg at 250 °C and 23 mmol/kg at 350 °C). The Si concentration started to decrease to the steady-state value when the Ca concentration increased to the maximum value (44–264 h at 250 °C, 17–71 h at 350 °C; Table 1).

Table 1. Concentration of selected species measured in fluids from experiments in the komatiite–H_2O–NO_3^- system.

	Time [h]	T [°C]	pH_{25} [a]	$pH_{in\text{-}situ}$ [b]	H_2 [m]	Cl [m]	Na [m]	K [m]	Mg [m]	Ca [m]	Si [m]	Fe [m]	Mn [m]	NH_4^+ [m]	NO_2^- [m]	NO_3^- [m]	N_2O [m]	Fluid [c] [g]
N250 (soln. = 72.4 g, rock = 9.64 g, P = 500 bars)																		
0		20	9		0.030	990	1014	0.28	0.339	0.3	0.1	0.02 [d]	n.d.	n.d.	n.d.	10.936	n.d.	72.4
1	0.0	235	9.6	7.7	0.030	986	991	0.32	0.009	2.7	2.5	0.02 [d]	n.d.	0.023	n.d.	10.748	n.d.	69.4
2	4	246	9.4	7.8	0.030	994	986	0.39	0.004	3.9	4.7	0.02 [d]	n.d.	0.030	0.009	10.534	0.002	65.2
3	8	250	8.4	7.6	0.030	986	980	0.39	0.002	4.2	5.7	0.02 [d]	n.d.	0.037	0.011	10.716	0.005	60.7
4	18	250	9.1	7.8	0.030	985	991	0.40	0.002	4.6	6.0	0.02 [d]	n.d.	0.056	0.011	10.286	0.011	56.3
5	44	250	8.8	7.7	0.030	1007	984	0.53	0.002	6.2	6.2	0.02 [d]	n.d.	0.101	0.009	10.132	0.009	52.2
6	264	250	8.9	6.2	0.030	1016	955	1.83	0.018	36.0	1.1	0.02 [d]	n.d.	1.140	n.d.	0.015	0.002	48.9
7	1054	250	8.8	5.9	0.030	1051	957	1.87	0.023	30.8	0.8	0.02 [d]	n.d.	1.168	n.d.	0.005	0.002	45.6
8	1944	250	8.6	5.6	0.585	1045	961	1.79	0.020	30.7	0.7	0.02 [d]	n.d.	1.192	n.d.	0.007	n.d.	42.2
9	2616	250	8.8	5.8	1.4	1043	961	1.81	0.020	30.4	0.7	0.02 [d]	n.d.	1.184	n.d.	0.006	n.m.	38.9
10	4871	250	8.6	5.6	2.3	1045	960	1.74	0.020	29.6	0.7	0.02 [d]	n.d.	1.174	n.d.	0.010	n.m.	35.4
N350 (soln. = 63.93 g, rock = 12.2 g, P = 500 bars)																		
0		25	8.5		0.031	989	992	0.85	0.588	1.3	0	0.01	0.001	0.002	n.d.	1.063	n.d.	63.9
1	0	350	7.2	7.1	0.019	1004	1006	1.01	0.037	3.8	18.1	0.03	0.001	0.085	n.d.	0.950	n.d.	60.9
2	17	350	6.3	5.8	0.006	999	973	1.07	0.011	10.4	20.5	0.01	0.004	0.132	n.d.	0.106	0.007	55.3
3	71	350	6.2	4.9	0.668	1004	929	1.73	0.197	37.8	2.9	0.18	0.087	0.180	n.d.	0.005	n.d.	50.3
4	187	350	6.1	4.9	1.941	1030	955	1.77	0.266	34.2	2.8	0.33	0.148	0.182	n.d.	0.003 [d]	n.d.	44.8
5	521	350	6.1	4.9	3.400	1020	956	2.04	0.39	23.8	3.0	0.27	0.104	0.176	n.d.	0.003	n.d.	39.9
6	2515	350	5.7	5.0	1.660	1026	967	2.10	0.24	23.1	2.8	0.27	0.086	0.171	n.d.	n.m.	n.d.	35.1

Concentrations are in mmol/kg [m]. n.d.—not detected. n.m.—not measured. [a] Measured pH at 25 °C. [b] Calculated $pH_{in\text{-}situ}$ at experimental temperature and 500 bars. [c] Estimated amount of fluid in the reaction cell prior to sampling. [d] Upper limit.

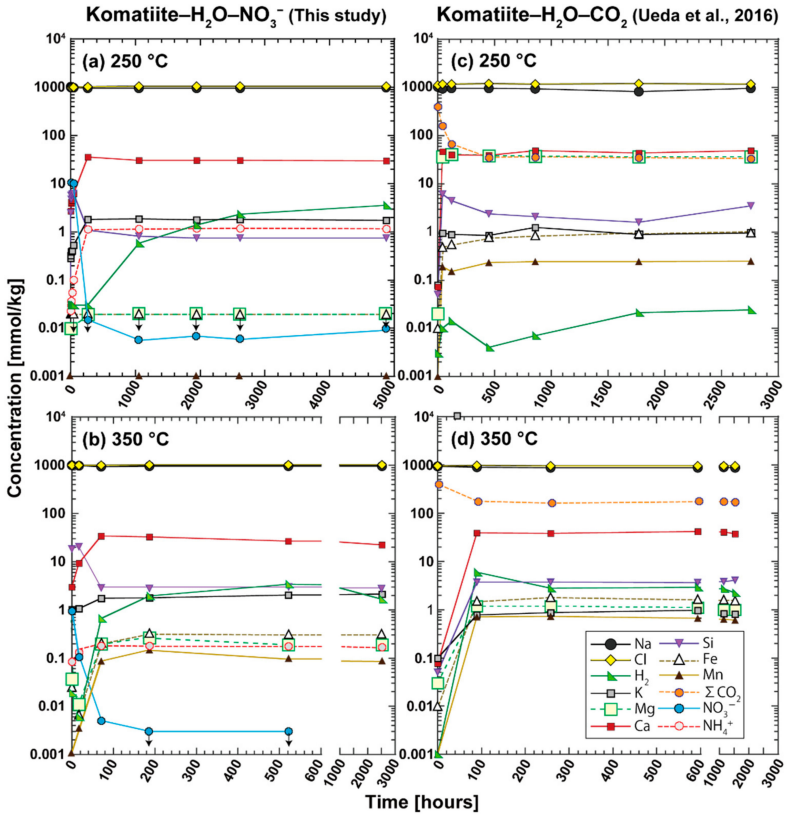

Figure 1. Measured concentrations of dissolved species in an aqueous fluid coexisting with komatiite and its alteration products as functions of time at 250 °C (**a**,**c**) and 350 °C (**b**,**d**), 500 bars. (**a**,**b**) Fluid compositions in the komatiite–H_2O–NO_3^- system at 250 °C and 350 °C with the initial water–rock mass ratios of 7 and 5, respectively. (**c**,**d**) Fluid compositions in the komatiite–H_2O–CO_2 system at 250 °C and 350 °C with the initial water–rock mass ratios of 5 and 5, respectively (Ueda et al., 2016). White triangles and light-blue circles with black arrows imply that iron and nitrate concentrations in plot are the maximum estimates (0.02 mmol/kg for iron in N250, 0.003 mmol/kg for nitrate in N350).

Nitrate concentrations decreased from 11 mmol/kg to approximately 0.01 mmol/kg after 264 h at 250 °C, and decreased from 1 mmol/kg to approximately 0.005 mmol/kg after 71 h at 350 °C. Over the same time interval, ammonium concentration increased from 0.02 mmol/kg to 1.14 mmol/kg at 250 °C and 0.08 mmol/kg to 0.18 mmol/kg at 350 °C. Nitrite concentration increased from less than 0.002 mmol/kg to 0.011 mmol/kg in the first 18 h and then decreased to less than 0.002 mmol/kg at 250 °C, whereas it was less than 0.002 mmol/kg throughout the experiment at 350 °C.

The time-dependent changes of nitrogen compounds suggest that a multi-step pathway exists for the reduction of nitrate to ammonia via nitrite at 250 °C. This is comparable to the biological process referred to as dissimilatory nitrate reduction to ammonia. The mol ratio of ammonia produced to nitrate reduced (i.e., the product yield) was estimated to be 10% at both 250 °C and 350 °C. Thus, the other 90% of nitrate initially present in the fluid is expected to be reduced to other nitrogen species, most likely N_2 via nitrous oxide (Section 4.2). The decrease in nitrate concentration appeared to be coupled with the increase in calcium concentration and with the decrease in $pH_{in\text{-}situ}$ at both 250 °C and 350 °C.

By comparison, experiments without komatiite show less reduction of nitrate at both 250 °C and 350 °C. In these experiments, nitrate concentrations were constant at 10 mmol/kg within the range of analytical uncertainty (±2%) and decreased slightly from 10 mmol/kg to 9 mmol/kg within 860 h and 264 h under 500 bars at 250 °C and 350 °C, respectively (Table 2, Figure 2). Over the same time intervals, nitrite concentration increased to 1.1 mmol/kg at 350 °C, whereas it was below detection limit at 250 °C. Nitrous oxide concentrations increased up to 0.01 mmol/kg and 0.05 mmol/kg at 250 °C and 350 °C, respectively. Ammonium concentrations were below the detection limit at both 250 °C and 350 °C. This indicates nitrate reduction to nitrite in the H_2O–NO_3^- system at 350 °C. However, the rate of nitrate reduction is more than 40 times slower than that in the komatiite–H_2O–NO_3^- system at 350 °C. Hence, komatiite causes or stimulates nitrate reduction and ammonia production in aqueous fluids at temperature above 250 °C and pressure of 500 bars.

Table 2. Concentration of selected species measured in fluids from experiments in the H_2O–NO_3^- system.

	Time [h]	T [°C]	pH_{25}	$pH_{in\text{-}situ}$	Cl [m]	Na [m]	K [m]	NH_4^+ [m]	NO_2^- [m]	NO_3^- [m]	N_2O [m]
N250C (P = 500 bars)											
0		22			970	958	10.0	n.d.	0.002	10.132	n.m.
1	22	250	8.7	5.6	1011	970	10.4	m.f.	0.002	10.329	0.001
2	213	250	8.8	5.7	999	950	10.0	m.f.	0.002	10.267	0.007
3	381	250	10	6.7	987	971	9.9	m.f.	0.002	10.234	0.006
4	860	250	9.4	6.2	998	962	10.1	n.d.	0.002	10.361	0.005
N350C (P = 500 bars)											
0		22	6.3		985	966	10.0	n.d.	0.005	10.205	0.000
1	0	339	9.9	6.6 [a]	983	n.m.	n.m.	n.d.	0.002	9.733	0.009
2	4	346	9.9	6.6 [a]	983	n.m.	n.m.	n.d.	0.122	9.919	0.013
3	8	349	10	6.7 [a]	980	n.m.	n.m.	n.d.	0.153	9.923	0.012
4	11	350	10	6.7 [a]	982	n.m.	n.m.	n.d.	0.196	9.819	0.010
5	21	350	9.8	6.5 [a]	986	n.m.	n.m.	n.d.	0.267	9.854	0.010
6	76	350	9.4	6.1 [a]	996	n.m.	n.m.	n.d.	0.404	9.434	0.010
7	264	350	9.5	6.2	1030	974	10.0	n.d.	1.103	9.137	0.005

Concentrations are in mmol/kg [m]. n.d.—not detected. n.m.—not measured. m.f.—measurement failed. [a] Calculated $pH_{in\text{-}situ}$ at experimental temperature and 500 bars assuming that Na and K concentrations in the sampled fluid are the same as those in the initial solution (Na = 966 mmol/kg, K = 10.0 mmol/kg).

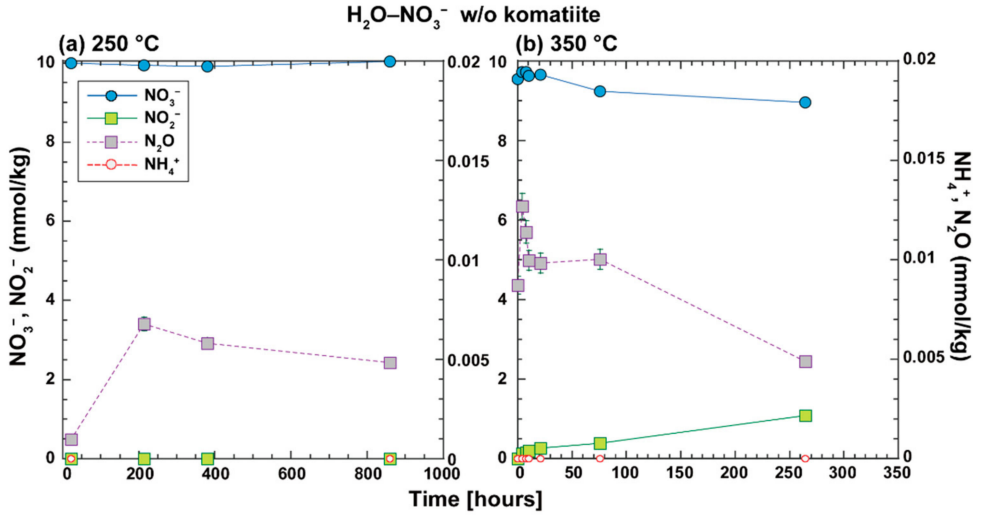

Figure 2. Mole fractions of nitrate, nitrite, nitrous oxide, and ammonia in aqueous fluids without komatiite at (**a**) 250 °C and (**b**) 350 °C. Measured concentrations of nitrogen species at a given time are normalized by the initial concentration of nitrate (10 mmol/kg) to estimate the mole fractions. For each plot, Y axis on the left side shows the scale of the mole fractions of nitrate and nitrite, whereas that on the right side shows the scale of the mole fractions of nitrous oxide and ammonia.

The dissolved H_2 concentration increased to steady-state values of 2.3 and 1.7 mmol/kg at 250 °C and 350 °C, respectively. By comparison, steady-state concentrations of the dissolved H_2 concentration in the komatiite–H_2O–CO_2 system were reported to be 0.02 mmol/kg and 2 mmol/kg at 250 °C and 350 °C, respectively (Figure 3) [50]. The steady-state concentration of dissolved H_2 in the komatiite–H_2O system was reported to be 23 mmol/kg at 300 °C [49]. Table 3 compares the steady-state composition of fluids in the komatiite–H_2O–NO_3^- system with that in the komatiite–H_2O–CO_2 system, as reported by [50]. Besides H_2, the remarkable differences between the aqueous fluids in the two systems are the steady-state concentrations of Mg, and Fe and fluid pH at 250 °C. The dissolved Mg and Fe concentrations in the komatiite–H_2O–NO_3^- system are 2–3 orders of magnitude lower than those in the komatiite–H_2O–CO_2 system. The pH measured at room temperature in the komatiite–H_2O–NO_3^- system is more alkaline than that in the komatiite–H_2O–CO_2 system.

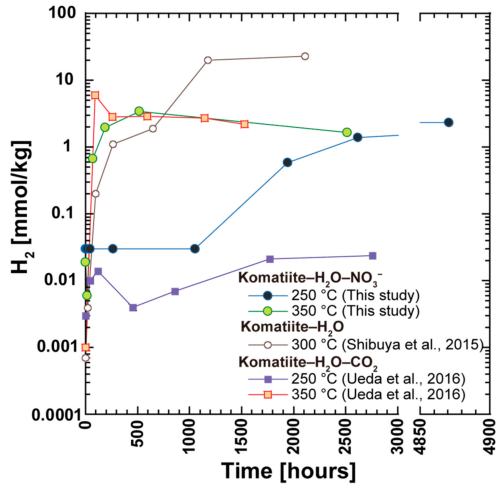

Figure 3. Time-dependent changes in dissolved H_2 concentrations in aqueous fluids in the systems of komatiite–H_2O–NO_3^- (this study), komatiite–H_2O–CO_2 [50], and komatiite–H_2O [49].

Table 3. Steady-state composition of aqueous fluids in the komatiite–H_2O–NO_3^- and komatiite–H_2O–CO_2 systems.

System	Komatiite-H_2O-NO_3^-		Komatiite-H_2O-CO_2	
Experiment ID	**N250**	**N350**	**U250** [b]	**U350** [b]
T [°C]	250	350	250	350
P [bar]	500	500	500	500
Reaction time [hours]	4871	2515	2760	1530
$(water/rock)_{final}$ [a]	3.7	2.9	3	3
$pH_{25°C}$	8.7	6.0	4.5	3.9
$pH_{in\text{-}situ}$	5.8	5.0	4.8	5.7
H_2 [m]	2.3	1.7	0.02	2.2
ΣCO_2 [m]	n.m.	n.m.	33	171
Cl [m]	1045	1026	1175	953
Na [m]	960	967	949	884
K [m]	1.74	2.10	0.95	0.81
Mg [m]	≤0.02	0.24	36.4	1
Ca [m]	30	23	48.8	37.3
Si [m]	0.74	2.81	3.5	4.1
Fe [m]	≤0.02	0.27	0.97	1.55
Mn [m]	≤0.001	0.086	0.25	0.6
NH_4^+ [m]	1.174	0.171	n.m.	n.m.
reference	This study	This study	[50].	[50]

Concentrations are in mmol/kg [m]. n.m.—not measured. [a] Water–rock mass ratio. [b] Initial aqueous solutions were prepared with the following chemical composition: 1000 mmol/kg Cl, 1000 mmol/kg Na, and 400 mmol/kg ΣCO_2. The pH values of the initial solutions were ~4.9 at room temperature.

3.2. Alteration Products

The characterization of the solid products of the komatiite alteration experiments at 250 °C and 350 °C by X-ray diffraction, Raman spectroscopy, EPMA and SEM/EDX indicates that the products were dominated by a mixture of smectite, chlorite, and serpentine, and/or mixed layer clays such as chlorite/smectite and chlorite/serpentine (Figures 4 and 6 and Tables 4 and 5). Andradite and clinopyroxene were observed as characteristic major components at 250 °C and 350 °C, respectively. The reaction products exhibited the following characteristics:

1. The reaction products at 250 °C and 350 °C were mainly composed of 10–50-μm-size clusters of mineral plates/flakes. The plates/flakes developed an edge-to-face pattern and/or a rosette-like pattern (Figures 5e and 7d,g). Such patterns are observed for the plates/flakes of chlorite, smectite and corrensite (mixed layered chlorite-smectite mineral) coated on a variety of silicate minerals in natural and experimental systems, e.g., [63–65]. Raman spectra of the clusters separated as the yellowish green or greenish grains from the bulk products showed peaks attributable to smectite, chlorite, serpentine and vermiculite (mixed layered chlorite-smectite mineral) (Figure 6h-1,h-3). The clusters also showed intermediate compositions between smectite (saponite), chlorite (clinochlore), and serpentine (Tables 4 and 5). Collectively, we interpreted that the mineralogy of the clusters was a mixture of smectite, chlorite, and serpentine, and/or mixed layer clays such as chlorite/smectite and chlorite/serpentine (Table 4).
2. The clusters at both 250 °C and 350 °C had overgrowth rims extending outward from the center (Figure 5a,b and Figure 7a,b). The rims were composed of slightly curved flakes that developed honeycomb patterns with pore of 1–2 μm and 2–3 μm in size at 250 °C and 350 °C, respectively (Figures 5c and 7b). Moreover, overgrowth rims with frost column textures partly covered the surface of the cluster at 250 °C (Figure 5e). There were not marked differences in elemental ratios between the rims and the phyllosilicate clusters at both 250 °C and 350 °C, suggesting that the rims had the same mineral composition as the clusters (Table 5).
3. Spherical (polygonal) minerals (ca. 1–3 μm in size) were found in the reaction products at 250 °C (Figures 5e and 7a,b,f). They existed both in the cluster and the overgrowth

rims. These minerals were identified as andradite ($Ca_3Fe^{III}_2Si_3O_{12}$) based on their Raman spectra (Figure 6h-2). Results of the semi-quantitative analysis by SEM/EDX of the spherical minerals indicate elemental ratios that were consistent with those of andradite (Table 5).

4. Needle-shaped minerals occurred with the overgrowth rims in the reaction products at 350 °C (Figure 7a,b,f,h). The needles stuck together and formed an irregular-shaped, opaque grain that was separated as an unsuspended fraction after sonication (Figure 6d,g and Figure 7f). Raman spectra of these opaque grains indicated that the needles were clinopyroxene (Figure 6h-4). Semi-quantitative analysis by SEM/EDX of the needles showed elemental ratios that were consistent with clinopyroxene (Table 5).
5. Fibrous minerals were observed in the reaction products at 350 °C (Figure 7c,d). Regarding their morphology, they could be chrysotile fibers.
6. Needle-shaped calcium silicate occasionally occurred with andradite in the reaction products at 250 °C (Figure 5h). SEM/EDX analysis shows Ca/Si over 1 with Mg + Fe/Si smaller than 0.5 (Table 5). Clinopyroxene was also found among the reaction products at 250 °C as a minor component.

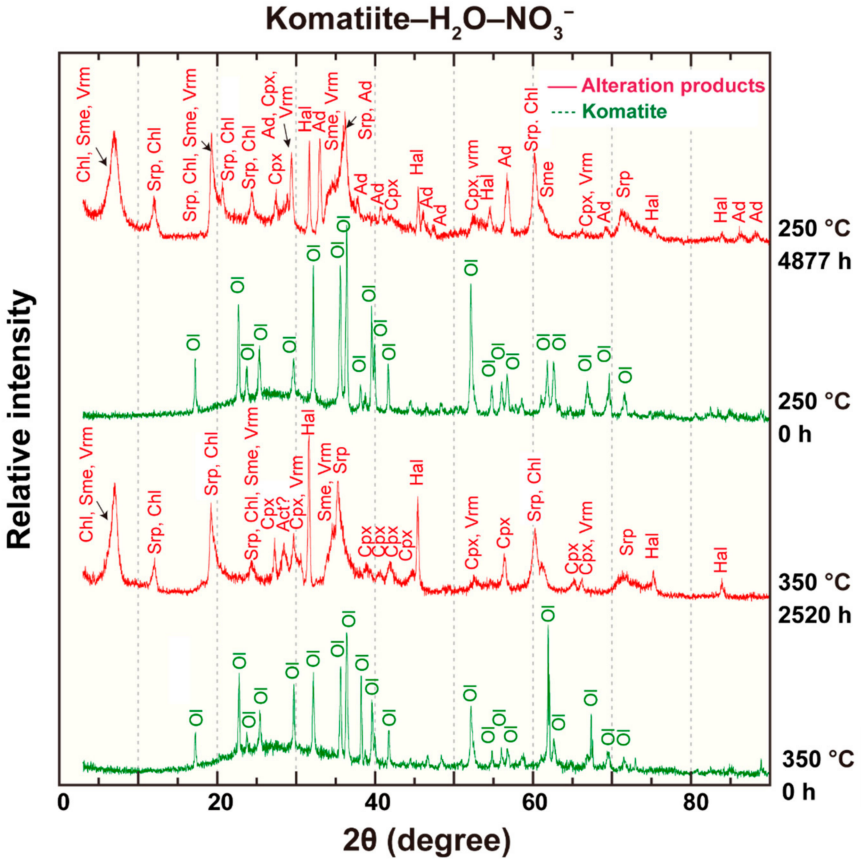

Figure 4. Powder XRD patterns (CuKα) of the alteration products after experiment N250 (250 °C, 4877 h) and N350 (350 °C, 2520 h), denoted by red. For comparison, XRD patterns (CuKα) of the synthetic komatiite used in the experiments are presented in green. The mineral identified from the XRD patterns of the synthetic komatiite is ferroan forsterite with a mole (Mg/Fe) ratio of ~9. Abbreviations are the same as in Table A1.

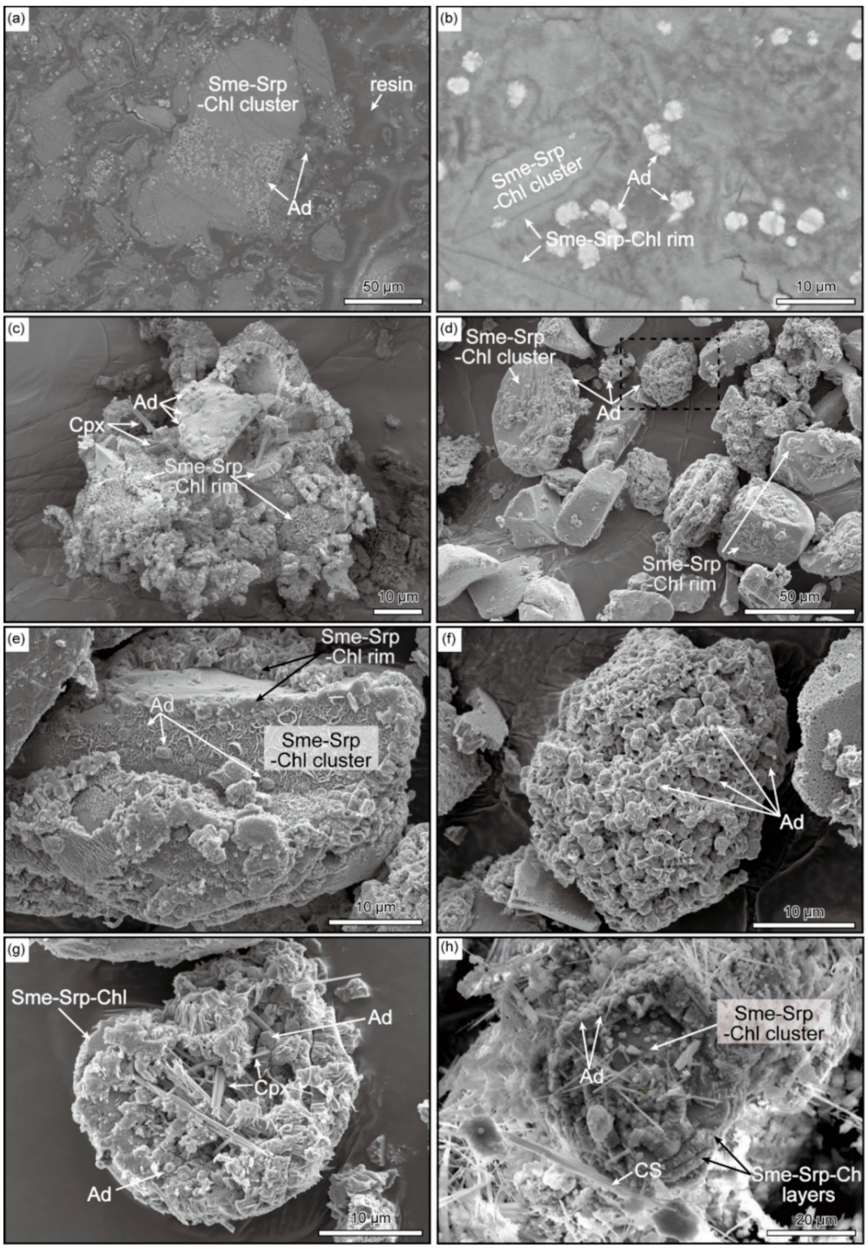

Figure 5. Representative SEM images of alteration products after experiment N250 (250 °C, 4877 h). (**a**,**b**) Polished sample mounted on epoxy resin showing 10–50 μm-size clusters comprising phyllosilicates (smectite, serpentine, and chlorite: Sme-Srp-Chl) in the core with overgrowth rims of phyllosilicates and bright spherical andradite. The dark portion of these panels is epoxy resin. (**c**) Aggregate of crushed samples showing various morphologies of individual grains. (**d**–**g**) SEM images of the unsuspended fraction separated from bulk products by sonication with water and ethanol (**d**) Clusters of phyllosilicates that are partially covered by phyllosilicates with frost column textures and/or andradite. (**e**) Cluster of phyllosilicates. The core of the cluster comprises plates/flakes that develops an edge-to-face pattern and/or a rosette-like pattern, whereas the rim shows frost column texture. (**f**) Enlarged view of a dashed black frame in (**d**) showing botryoidally aggregated andradite spheres overgrown on the surface of phyllosilicate cluster. (**g**) Spherical aggregate comprising clinopyroxene needles, andradite spheres, and phyllosilicates. (**h**) Cross sectional view of phyllosilicate cluster covered by phyllosilicate layers. Spherical andradite crystals occur with needle-like calcium silicate (CS) at the surface of the upper most layer of phyllosilicates. Abbreviations are the same as in Table A1.

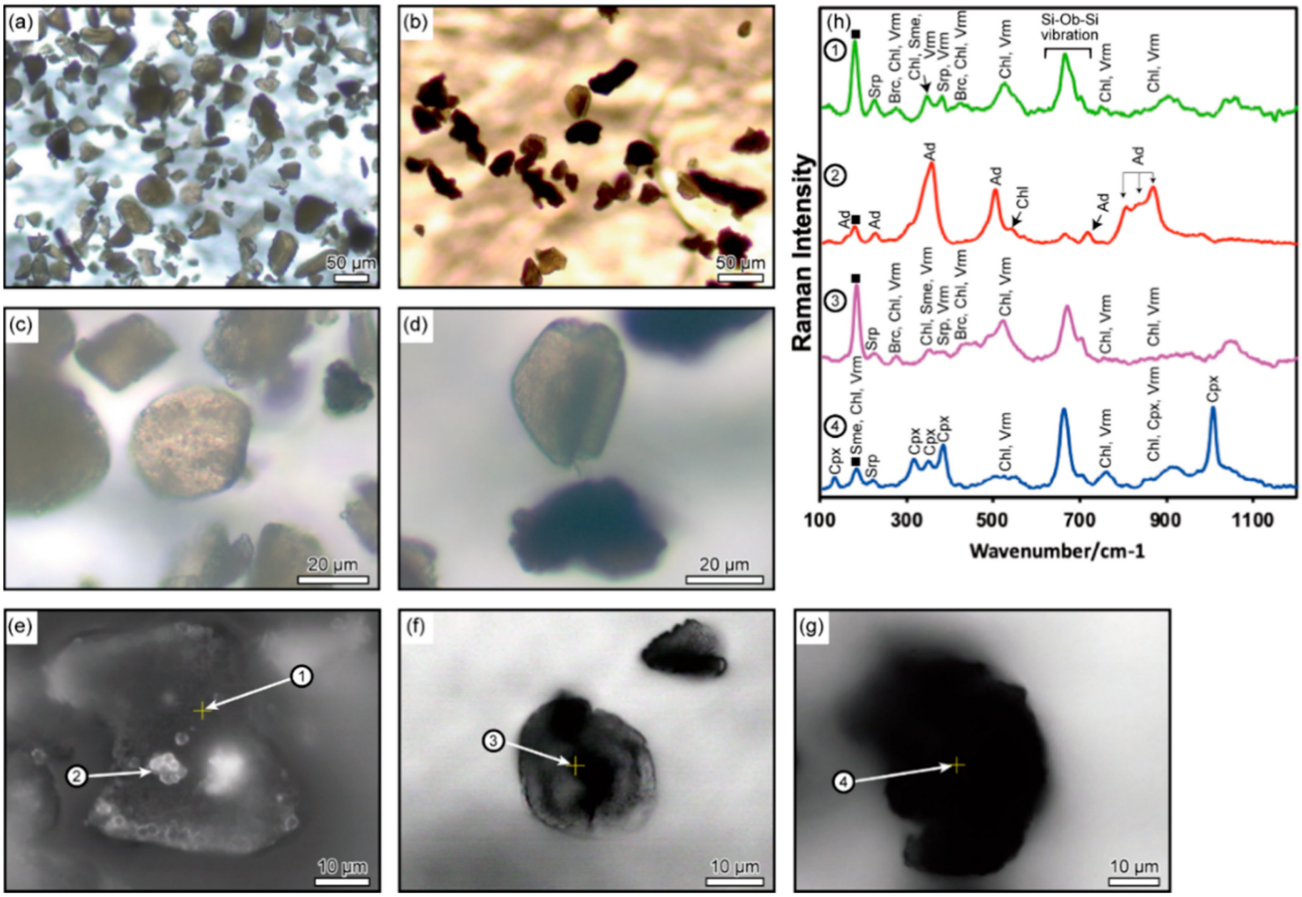

Figure 6. Optical microscopy images and Raman spectra of grains in unsuspended fractions separated from the bulk products at 250 °C and 350 °C. (**a**,**c**,**e**) Photomicrographs of an unsuspended fraction in experiments N250 (250 °C, 4877 h) showing yellowish green grains (10–50 μm in size). Small spherical grains (ca. 1 μm in size) are often found on the surface of yellowish green grains. (**b**,**d**,**f**,**g**) Photomicrographs of an unsuspended fraction in experiment N350 (350 °C, 2520 h) showing two types of grains: rounded greenish grains (20–50 μm in size) and random-shaped opaque grains (20–50 μm in size). Numbers in Figure 6e–g; correspond to those shown in Figure 6h. (**h**) Representative Raman spectra. Raman spectra of the yellowish green grains of N250 and the greenish grains of N350 (numbers 1 and 3) show peaks attributable to smectite, chlorite, actinolite, and serpentine that have nearly the same wavenumber. Raman spectra of the small spherical grains of N250 (number 2) show peaks attributable to andradite. Raman spectra of the random-shaped opaque grains of N350 (number 4) show the peaks attributable to clinopyroxene. A large peak between 650 cm^{-1} and 700 cm^{-1} is common in inosilicate and phyllosilicate candidates. Abbreviations in Figure 6h are the same as in Table A1.

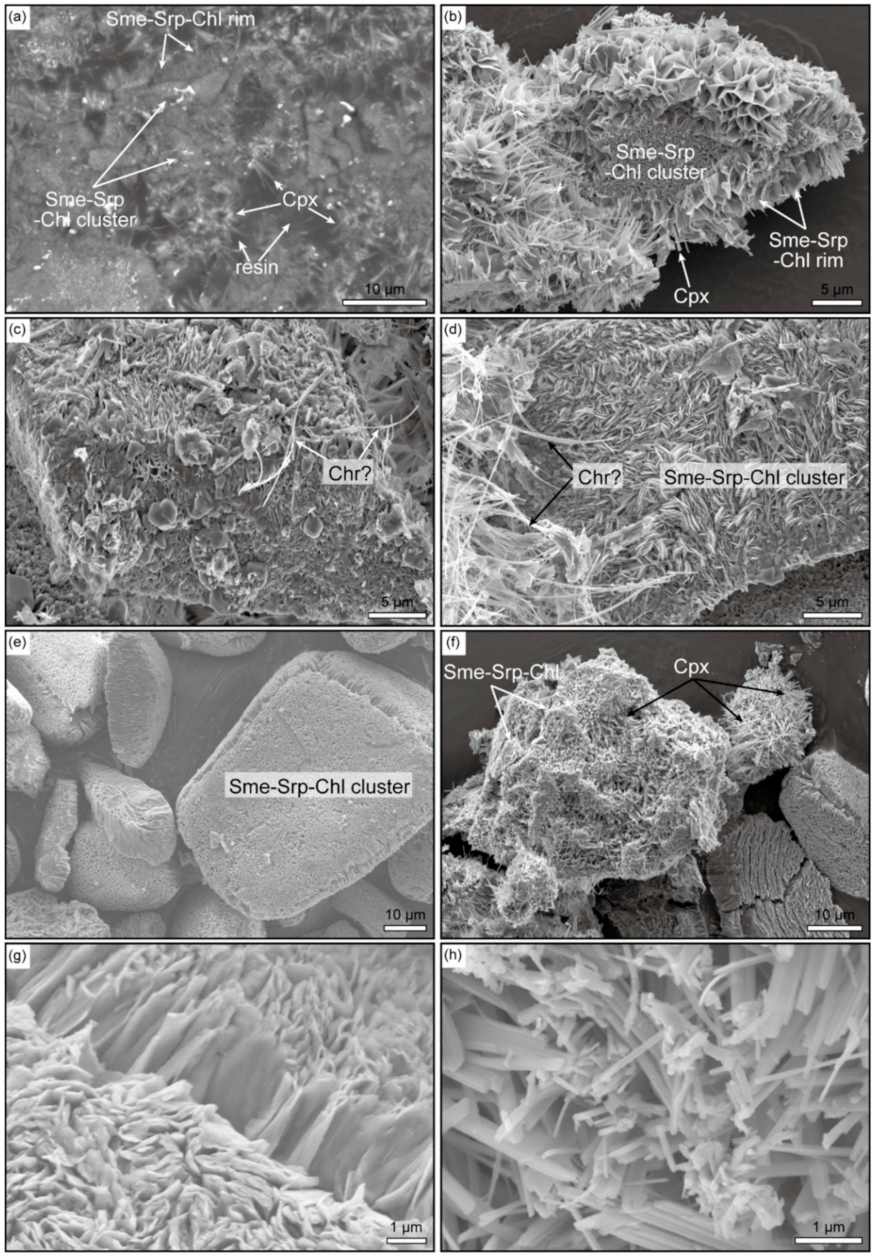

Figure 7. Representative SEM images of alteration products after experiment N350 (350 °C, 2520 h). (**a**) A polished sample mounted on epoxy resin showing clusters of phyllosilicates (smectite, serpentine, and chlorite) in the core with overgrowth rims of phyllosilicates and needle-like crystals of clinopyroxene. The dark portion of the panel is epoxy resin. (**b**–**d**) SEM images of crushed samples. (**b**) Cluster of phyllosilicates. The core of the cluster comprises plates/flakes that develop an edge-to-face pattern and/or a rosette-like pattern, whereas the rim shows honeycomb texture with 2–3 µm pores. Needle-shaped clinopyroxene occurs with overgrowth rims of phyllosilicates. (**c**,**d**) Cluster of phyllosilicates with an unidentified polygonal mineral and a fibrous mineral that is presumed to be chrysotile. (**e**,**f**) Unsuspended fraction showing rounded clusters comprising phyllosilicates (**e**) and irregular-shaped clusters comprising clinopyroxene and phyllosilicates (**f**). (**g**) Enlarged view of a phyllosilicate cluster. Plates/flakes develop an edge-to-face pattern. (**h**) Enlarged view of needle-shaped clinopyroxene. Abbreviations are the same as in Table A1.

Table 4. Composition of synthetic komatiite and solid reaction products from the experiments in the komatiite–H_2O–NO_3^- system at 250 °C and 350 °C (values in wt.%).

	Al-Depleted Synthetic Komatiite			N250		N350		Reference Minerals (Ideal Composition)		
	WR	**Ol**	**Glass**	**Clst 1**	**Clst 2**	**Clst 1**	**Clst 2**	**Sap**	**Srp**	**Clin**
SiO_2	46.70	41.11	51.70	41.06	39.75	38.84	40.64	44.11	41.01	32.42
TiO_2	0.38	0.03	0.50	0.13	0.41	0.08	0.94			
Al_2O_3	3.7	0.04	5.49	1.17	4.03	5.68	3.85	5.35		18.24
Cr_2O_3	n.m. (0.35)	0.16	0.32	0.56	0.46	0.25	0.21			
FeO	11.43	7.02	10.94	11.13	10.58	10.21	8.71	7.54	12.26	
MnO	0.18	0.13	0.22	0.30	0.30	0.14	0.09			
MgO	29.89	49.80	18.83	25.59	23.18	27.68	21.39	21.14	34.40	36.25
CaO	7.26	0.23	9.93	0.71	2.83	0.28	3.14	2.94		
Na_2O	0.06	0.01	0.25	≤0.65	≤0.84	≤0.47	≤0.94			
K_2O	n.d. (0.03)	0.01	0.00	n.d.	0.004	n.d.	0.017			
NiO	n.m. (0.19)	0.19	0.07	0.05	0.07	0.08	0.12			
P_2O_5	0.04	n.d.	0.02	n.d.	0.006	n.d.	n.d.			
Total	99.63	98.70	98.23	81.35	82.47	83.70	80.06	81.07	87.67	87.00
Method	XRF	EPMA	EPMA	EPMA	EPMA	EPMA	EPMA	calc.	calc.	calc.
Note				Ca-poor	Ca-rich	Ca-poor	Ca-rich			

n.m.—not measured. n.d.—not detected. cal.—calculation. Values in parentheses are target concentrations. Srp = $Mg_5FeSi_4O_{10}(OH)_8$. Abbreviations are the same as in Table A1 except for WR (=whole rock) and Clst (=Cluster).

Table 5. Representative elemental compositions measured using SEM/EDS (atom number %).

			N250			
Morphology	**Cluster**	**Frost Column** [a]	**Polygonal**	**Needle**	**Needle**	**Columnar**
Interpretation	**Sme-Srp-Chl**	**Sme-Srp-Chl**	**Andradite**	**Augite**	**Wollastonite**	**Calcium Silicate**
(Mg + Fe)/Si	1.32	1.04	0.72	0.81	0.23	0.42
Fe/Fe + Mg	0.12	0.12	0.79	0.19	0.13	0.67
Ca/Si	0.07	0.04	1.06	0.40	1.24	3.10
Al/Si	0.14	0.10	0.07	0.05	0.02	0.02
			N350			
Morphology	**Cluster**	**Flake** [b]	**Needle**	**Needle**		
Interpretation	**Sme-Srp-Chl**	**Sme-Srp-Chl**	**Augite**	**Augite**		
(Mg + Fe)/Si	1.27	1.14	0.58	0.74		
Fe/Fe + Mg	0.33	0.11	0.28	0.20		
Ca/Si	0.04	0.04	0.51	0.34		
Al/Si	0.12	0.13	0.04	0.04		

[a] Secondary mineral partly covering the surface of the cluster. [b] Mineral flakes covering the surface of the cluster in honeycomb pattern. Abbreviations are the same as in Table A1.

Based on the petrographic observations described above, clinopyroxene deposited after the formation of smectite–serpentine–chlorite core assemblage at 350 °C.

4. Discussion

4.1. Water-Rock Interactions in the Komatiite–H_2O–NO_3^- System

Fluid composition and secondary mineral assemblages provide information on the water-rock interactions that include hydrogen generation and nitrate reduction. To aid the interpretation of reactions occurring during the experiments, saturation indexes of solid materials were calculated based on the measured fluid composition (Table 6). A list of potential water-rock reactions is also shown in Table 7.

Table 6. Saturation indexes of selected solid materials co-existing with fluids from experiments in the komatiite–H_2O–NO_3^- system.

	Time [h]	T [°C]	SiO_2 (am)	For	Faya [a]	Chry	Mgt [a]	Ad [a]	Diop	Wol
					N250					
1	0	235	−1.1	2.6	2.7	6.5	6.2	10.2	4.5	0.8
2	4	244	−0.9	2.7	2.5	6.6	5.7	12.0	5.3	1.6
3	8	250	−0.7	1.7	2.8	5.2	6.1	11.6	4.6	1.4
4	18	250	−0.8	2.3	2.3	6.0	5.4	12.5	5.4	1.8
5	44	250	−0.8	2.1	2.5	5.7	5.7	12.7	5.3	1.8
6	264	250	−1.3	−1.6	1.8	−0.1	5.6	4.1	0.3	−1.0
7	1054	250	−1.5	−2.8	0.5	−2.0	3.8	0.2	−1.3	−1.9
8	1944	250	−1.5	<−3	−0.5	<−3	1.0	<−3	−2.5	−2.5
9	2616	250	−1.5	<−3	0.1	−2.9	1.6	−2.6	−1.8	−2.2
10	4871	250	−1.5	<−3	−0.5	<−3	0.5	<−3	−2.5	−2.5
					N350					
1	0	350	−0.3	4.8	2.9	8.4	6.7	11.0	5.7	1.2
2	17	350	−0.2	0.2	−0.4	1.6	2.4	2.3	1.4	−0.8
3	71	350	−1.1	−1.6	−2.4	−1.5	−1.4	<−3	−2.0	−2.9
4	187	350	−1.1	−1.4	−1.9	−1.3	−1.2	<−3	−2.0	<−3
5	521	350	−1.1	−1.0	−2.1	−0.7	−1.7	<−3	−2.0	<−3
6	2515	350	−1.1	−1.5	−2.1	−1.4	−1.4	<−3	−2.3	<−3

Saturation index calculated from the concentration of dissolved species listed in Table 1. [a] Saturation index during each time interval in experiment N250 lists the upper limit because Table 1 lists the upper limit of the dissolved iron concentration during each time interval in N250. Abbreviations are the same as in Table A1.

Table 7. List of water-rock reactions.

Reaction	#
1. Silicate formation from solid components MgO, Al_2O_3, and FeO	
$0.25Ca^{2+} + 2.5MgO_{rock} + 0.5FeO_{rock} + 0.25Al_2O_{3rock} + 3.5SiO_{2(aq)} + 5.25H_2O$ $= Ca_{0.25}(Mg_{2.5}Fe_{0.5})(Si_{3.5}Al_{0.5})O_{10}(OH)_2{\cdot}4H_2O$ [Saponite] $+ 0.5H^+$	(1)
$5MgO_{rock} + FeO_{rock} + 4SiO_{2(aq)} + 14H_2O = Mg_5FeSi_4O_{10}(OH)_8$ [Serpentine]	(2)
$5MgO_{rock} + 0.5Al_2O_{3rock} + 3SiO_{2(aq)} + 23H_2O = (Mg_5Al)(Si_3Al)O_{10}(OH)_8$ [Clinochlore]	(3)
$3Ca^{2+} + 2FeO_{rock} + 3SiO_{2(aq)} + 4H_2O = Ca_3Fe^{III}{}_2Si_3O_{12}$ [Andradite] $+ H_{2(aq)} + 6H^+$	(4)
$Ca^2 + MgO_{rock} + 2SiO_{2(aq)} + H_2O = CaMgSi_2O_6$ [Diopside] $+ 2H^+$	(5)
2. Silicate formation from dissolved species	
$0.25Ca^{2+} + 2.5Mg^{2+} + 0.5Fe^{2+} + 0.5\ Al^{3+} + 3.5SiO_{2(aq)} + 9H_2O = Ca_{0.25}(Mg_{2.5}Fe_{0.5})\ (Si_{3.5}Al_{0.5})O_{10}(OH)_2{\cdot}4H_2O + 8H^+$	(6)
$5Mg^{2+} + Fe^{2+} + 4SiO_{2(aq)} + 10H_2O = Mg_5FeSi_4O_{10}(OH)_8 + 12H^+$	(7)
$5Mg^{2+} + 2Al^{3+} + 3SiO_{2(aq)} + 12H_2O = (Mg_5Al)(Si_3Al)O_{10}(OH)_8 + 16H^+$	(8)
$3Ca^{2+} + 2Fe^{2+} + 3SiO_{2(aq)} + 6H_2O = Ca_3Fe^{III}{}_2Si_3O_{12} + 10H^+ + H_{2(aq)}$	(9)
$Ca^{2+} + Mg^{2+} + 2SiO_{2(aq)} + 2H_2O = CaMgSi_2O_6 + 4H^+$	(10)
$Ca^{2+} + SiO_{2(aq)} + H_2O = CaSiO_3$ [Wollastonite] $+ 2H^+$	(11)
3. Iron oxidation	
$Fe^{2+} + H_2O = Fe^{3+} + OH^- + 0.5H_{2(aq)}$	(12)
$3FeO_{rock} + H_2O = Fe_3O_4$ [Mgt] $+ H_{2(aq)}$	(13)
$2FeO_{rock} + 2SiO_{2(aq)} + 3H_2O = Fe^{III}{}_2Si_2O_5(OH)_4$ [Fe^{III}-srp] $+ H_{2(aq)}$	(14)
4. Dissolution of solid components	
$CaO_{rock} + 2H^+ = Ca^{2+} + H_2O$	(15)
$FeO_{rock} + 2H^+ = Fe^{2+} + H_2O$	(16)
$MgO_{rock} + 2H^+ = Mg^{2+} + H_2O$	(17)
$Al_2O_{3rock} + 3H_2O = 2Al^{3+} + 6OH^-$	(18)

In experiment N250, the concentration of dissolved Si ($SiO_{2(aq)}$) increased to the maximum value (6 mmol/kg) during the first 8 h at 250 °C and then, remained at the maximum value from 8 h to 44 h (Figure A1). The maximum concentration of $SiO_{2(aq)}$ was 15% of the $SiO_{2(aq)}$ concentration predicted from the solubility of amorphous silica (Table 6), but it was ~100 times higher than the $SiO_{2(aq)}$ concentration under olivine dissolution at

temperatures from 230 °C to 320 °C and ap$H_{in\text{-}situ}$ of 8 [66]. Moreover, the positive SI values of forsterite and fayalite after the first 44 h (i.e., supersaturation with respect to forsterite) indicates that olivine dissolution had been inhibited in the first 44 h (Table 6). Therefore, the water-rock interactions that mainly occurred from 8 h to 44 h are predicted to be the dissolution of komatiite glass and the precipitation of secondary silicates. Given the low solubility of Al_2O_3 [67] and the fact that the sampled fluids had low concentrations of Mg and Fe, the precipitation of secondary silicates may have largely occurred through reactions involving solid phases of komatiite glass (rxns. 1–3 in Table 7). This inference is supported by the stable $pH_{in\text{-}situ}$ value in the first 44 h because reactions 1 to 3 did not affect $pH_{in\text{-}situ}$ much as compared with silicate formation from dissolved species (rxns. 6–8).

The time interval between 44 h to 264 h was characterized by the decrease in $SiO_{2(aq)}$ concentrations from the maximum value to the steady state value and the decrease in $pH_{in\text{-}situ}$ from 7.7 to 6.2. The decrease in the $SiO_{2(aq)}$ concentration suggests the completion of the dissolution of the SiO_2 component in komatiite glass and the precipitation of secondary silicates. In particular, the decrease in $pH_{in\text{-}situ}$ requires the precipitation of dissolved Ca as Ca-bearing silicates (saponite, andradite, Ca-pyroxene) (rxns. 1, 4, 5) because the dissolved Ca concentration was high at the milli-molal level, while the dissolved concentrations of Mg and Fe were low over the same time interval. The precipitation of Ca-bearing silicates was consistent with the positive SI values of andradite and diopside ($CaMgSi_2O_6$) over the same time interval (Table 6). On the other hand, this was apparently inconsistent with the increase in the dissolved Ca concentration from 6 to 36 mmol/kg. This discrepancy can be resolved if the decrease in $pH_{in\text{-}situ}$ promoted the dissolution of the CaO component in glass (rxn. 15). Because andradite precipitation involves iron oxidation and H_2 generation (rxn. 4), this reaction probably induced nitrate reduction between 44 h to 264 h (Section 4.2). The oxidation of the FeO component in komatiite glass also possibly contributed to H_2 generation and nitrate reduction between 44 h to 264 h (rxns. 13–14).

The last interval between 264 h to 4871 h was characterized by the decrease in the Ca concentration to the steady state value (30 mol/kg; 266 h to 1054 h) and the increase in the H_2 concentration to 2 mmol/g. The decrease in the Ca concentration was attributed to the formation of andradite because the SI value of andradite was positive until 1054 h, whereas the SI value of diopside became negative after 264 h (Table 6). This suggests that andradite formation had produced H_2 until 1054 h. On the other hand, dissolution of fayalite, as inferred from the saturation of fluid with respect to fayalite since 1054 h (SI = 0), may have produced H_2 since 1054 h by the oxidation of the FeO component in olivine (FeO_{ol}) with water to form magnetite and/or Fe^{III}-bearing serpentine (rxns. 13–14) [68].

In experiment N350, the $SiO_{2(aq)}$ concentration in the first 17 h at 350 °C had the maximum value (20 mmol/kg), that is 63% of the $SiO_{2(aq)}$ concentration predicted from the solubility of amorphous silica (Figure A1). Over the same time interval, $pH_{in\text{-}situ}$ decreased from 7.1 to 5.8, whereas the Ca concentration increased to 10 mmol/kg. As discussed above, this suggests the dissolution of komatiite glass coupled with the formation of secondary silicates, which includes the precipitation of dissolved Ca as Ca-bearing silicates (saponite, Ca-pyroxene) (rxns. 1–5).

Subsequently, the $SiO_{2(aq)}$ concentration decreased from the maximum value to the steady state value (1 mmol/kg) from 17 h to 71 h. The decrease in the $SiO_{2(aq)}$ concentration was accompanied by a decrease in $pH_{in\text{-}situ}$. Thus, this time interval was probably characterized by the complete consumption of the SiO_2 component in komatiite glass and the precipitation of secondary silicates, including Ca-bearing silicates, which is consistent with the positive SI value of diopside at 17 h.

A main feature of the time interval between 71 h to 2515 h was the increase in the H_2 concentration to 3 mmol/kg. The SI values of secondary minerals predicted that H_2 generation during the entire interval of N350 can be driven by the oxidation of dissolved and solid phases of ferrous iron ($Fe^{2+}{}_{(aq)}$, FeO_{rock} = FeO_{glass}, FeO_{ol}) to form magnetite and/or Fe^{III}-bearing serpentine (rxns. 13–14). Because nitrate reduction to ammonia was

completed by 71 h, H_2 produced from iron oxidation may have been completely and/or partially consumed to reduce nitrate before 71 h.

4.2. Mechanisms of Nitrate Reduction to Ammonia and Denitrification in the Komatiite–H_2O–NO_3^- System

This study strongly suggests that reactions in komatiite cause the complete reduction of nitrate to N_2 and NH_3 with a ratio of $N_{2(aq)}/NH_{3(aq)}$ of 4.5 at both 250 °C and 350 °C, under pressures of 500 bars (Figure 8). The thermodynamic equilibrium of dissolved nitrogen species in the N–H–O system was evaluated first as a possible explanation for the $N_{2(aq)}/NH_{3(aq)}$ ratio to characterize the mechanism of nitrate reduction in hydrothermal environments.

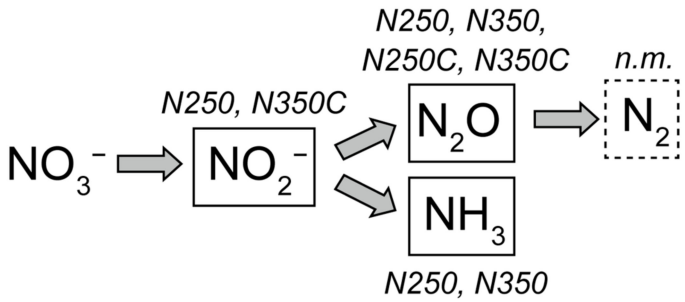

Figure 8. Model of abiotic nitrate reduction processes. Nitrite and nitrous oxide were detected as intermediate products during abiotic nitrate reduction in the komatiite–H_2O–NO_3^- and H_2O–NO_3^- systems. By contrast, ammonia was detected as an end product of abiotic nitrate reduction in the komatiite–H_2O–NO_3^- system ("chemoammonification"), but not in the H_2O–NO_3^- system. N_2 is thought to be another end product of abiotic nitrate reduction via nitrous oxide ("chemodenitrification"). Nitrogen species detected by experiments are shown in square. Experiment IDs in which a given nitrogen species was detected are shown. The fact that nitrite remained undetected in N250C and N350 suggests that the rate of nitrite reduction is much faster than that of nitrate reduction to nitrite. n.m.—not measured.

Figure 9a,b show the $pH_{in\text{-}situ}$ and $aH_{2(aq)}$ (or $aO_{2(aq)}$) states of water with theoretically predicted stability fields of dissolved nitrogen species in thermodynamic equilibrium at 250 °C and 350 °C, 500 bars, respectively. The stability fields are drawn based on the activity of NH_4^+ in the final sampled fluid ($aNH_{3(aq)} = 10^{-3.228}$ and $10^{-3.98}$ at 250 °C and 350 °C, respectively). Bold red lines in the diagrams indicate the $pH_{in\text{-}situ}$ and $aH_{2(aq)}$ values at which the activity ratios of two nitrogen species ($NH_{3(aq)}$–NH_4^+, $NH_{3(aq)}$–$N_{2(aq)}$, NH_4^+–$N_{2(aq)}$, and $N_{2(aq)}$–NO_3^-) equal one in thermodynamic equilibrium. The $pH_{in\text{-}situ}$ and $aH_{2(aq)}$ values were plotted for all sampled fluids in the komatiite–H_2O–NO_3^- and H_2O–NO_3^- systems in these diagrams to compare the dominant nitrogen species in the experimental products with those from the thermodynamic prediction. Given that the very low H_2 concentrations of sampled fluids in the H_2O–NO_3^- systems were difficult to measure, the presumed $aH_{2(aq)}$ values were plotted in the diagrams assuming that sub-milli molal O_2 in the initial solutions was not consumed during the experiments at 250 °C and 350 °C (e.g., dissolved O_2 concentration is 0.2 mmol/kg in an air saturated seawater).

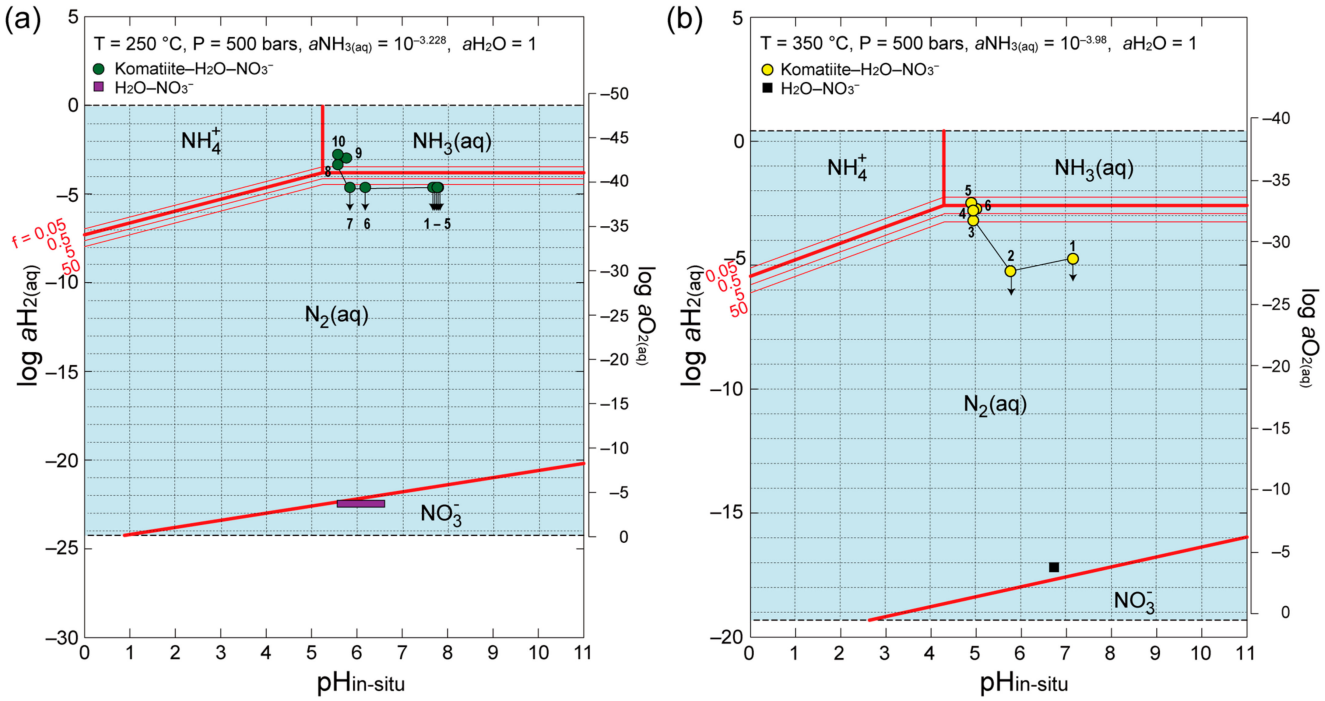

Figure 9. Diagrams of $pH_{in\text{-}situ}$ and $aH_{2(aq)}$ (or $aO_{2(aq)}$) with stability fields of nitrogen species in thermodynamic equilibrium at (**a**) 250 °C and (**b**) 350 °C, 500 bars. Bold red lines indicate the $pH_{in\text{-}situ}$ and $aH_{2(aq)}$ values at which the activity ratios of two nitrogen species follow the relations: $aNH_4^+/aNH_{3(aq)} = 1$, $aN_{2(aq)}/aNH_{3(aq)} = 0.5$, $aN_{2(aq)}/aNH_4^+ = 0.5$, or $aN_{2(aq)}/aNO_3^- = 0.5$. For the calculation, $aNH_{3(aq)}$ values were used in the final sampled fluids at 250 °C and 350 °C ($aNH_{3(aq)} = 10^{-3.228}$ and $10^{-3.98}$ at 250 °C and 350 °C, respectively). Thin, kinked red lines show the $pH_{in\text{-}situ}$ and $aH_{2(aq)}$ values at which the activity ratio of $aN_{2(aq)}/(aNH_{3(aq)} + aNH_4^+)$ is equal to 0.05, 5, and 50. Green and yellow circles indicate the fluid compositions in the komatiite–H_2O–NO_3^- system at 250 °C and 350 °C, respectively. The circles with black arrows imply that $aH_{2(aq)}$ in the plot is the maximum estimate. Numbers associated with green and yellow circles show sub-name of sampled fluids in experiments N250 and N350, respectively (Table 1). Purple and black boxes denote the fluid compositions in the H_2O–NO_3^- system at 250 °C and 350 °C, respectively (experiments N250C and N350C). Light blue areas in $pH_{in\text{-}situ}$–$aH_{2(aq)}$ spaces are the stability fields of water at 250 °C and 350 °C, respectively.

In the H_2O–NO_3^- system, sampled fluids at 250 °C and 350 °C were predicted to locate the stability fields of nitrate and N_2, respectively (purple and black boxes in Figure 9). In these experiments, nitrate at 250 °C was unreacted for 862 h, whereas nitrate at 350 °C was partially reduced for 264 h to nitrite and N_2O, which were expected to be reduced to N_2 via chemo-denitrification. The nitrate chemistry observed in the experiments is consistent with that predicted from the thermodynamic equilibrium of dissolved nitrogen species in the N–H–O system.

In the komatiite–H_2O–NO_3^- systems, sampled fluids at 250 °C and 350 °C evolved to have higher $aH_{2(aq)}$ values than that in the H_2O–NO_3^- systems, which are more favorable for ammonium production (green and yellow circles in Figure 9). The $N_{2(aq)}/NH_{3(aq)}$ ratios in thermodynamic equilibrium at the experimental $aH_{2(aq)}$ and $pH_{in\text{-}situ}$ conditions are estimated to be less than 50 for fluid samples taken during the interval of nitrate reduction at 250 °C (the first 264 h; N250-1–N250-6), whereas they increase from less than 5,000,000 to 50 for fluid samples taken during the first 264 h at 350 °C (N350-1–N350-3). Therefore, theoretical prediction assuming thermodynamic equilibrium of nitrogen species in N–H–O system underestimates the amount of $NH_{3(aq)}$ produced from nitrate in the komatiite–H_2O–NO_3^- systems by a factor of 10 and 10–1,000,000.

This suggests that nitrate reduction proceeds at the site of H_2 generation where local $aH_{2(aq)}$ is higher than $aH_{2(aq)}$ of bulk fluids (e.g., heterogeneous reaction at the solid surface). It is also possible that nitrate reduction is mainly driven by a reductant other than H_2.

Ferrous iron components in komatiite (FeO_{rock}) are potential candidates for reaction sites to reduce nitrate. A general H_2 generation reaction during serpentinization is written as iron oxidation reactions 14 and 15 in Table 7 [68]. In the komatiite–H_2O–NO_3^- systems at 250 °C, the H_2 generation reaction also occurs during andradite formation as discussed in Section 4.1 (rxn. 4). As discussed in Section 4.1, nitrate reduction in experiments N250 and N350 occurred during the time interval that was thermodynamically favorable to andradite formation (at 250 °C) and iron oxidation to form magnetite and/or Fe^{III}-bearing serpentine (at both 250 °C and 350 °C). Thus, we suggest the following reactions as nitrate reduction in the komatiite–H_2O–NO_3^- system (see Appendix A for details).

- Nitrate reduction during serpentinization (T = 250 °C and 350°C, P= 500 bars):

$$2NO_3^- + 2H^+ + 15FeO_{rock} = N_{2(aq)} + 5Fe_3O_4 + H_2O \quad (19)$$

$$2NO_3^- + 2H^+ + 24FeO_{rock} + 2H_2O = 2NH_{3(aq)} + 8Fe_3O_4 \quad (20)$$

$$2NO_3^- + 2H^+ + 10FeO_{rock} + 10SiO_{2(aq)} + 9H_2O = N_{2(aq)} + 5Fe^{III}{}_2Si_2O_5(OH)_4 \quad (21)$$

$$2NO_3^- + 2H^+ + 32FeO_{rock} + 32SiO_{2(aq)} + 40H_2O = 2NH_{3(aq)} + 16Fe^{III}{}_2Si_2O_5(OH)_4 \quad (22)$$

- Nitrate reduction coupled with andradite formation (T = 250 °C, P = 500 bars):

$$2NO_3^- + 15Ca^{2+} + 10FeO_{rock} + 15SiO_{2(aq)} + 14H_2O = N_{2(aq)} + 5Ca_3Fe^{III}{}_2Si_3O_{12} + 28H^+ \quad (23)$$

$$2NO_3^- + 24Ca^{2+} + 16FeO_{rock} + 24SiO_{2(aq)} + 26H_2O = 2NH_{3(aq)} + 8Ca_3Fe^{III}{}_2Si_3O_{12} + 46H^+ \quad (24)$$

The reactions 19 to 24 represent nitrate reduction by both H_2 and Fe^{II} at the site of serpentinization and andradite formation. They probably contribute to a lower $N_{2(aq)}/NH_{3(aq)}$ ratio in the komatiite–H_2O–NO_3^- system than expected due to the thermodynamic equilibrium of dissolved nitrogen species in N–H–O system at 250 °C and 350 °C, 500 bars.

4.3. H_2 Generation Ability of Komatiite-Hosted Hydrothermal System in Early Earth

Previous simulations of komatiite hydrothermal alteration in the early ocean [49,50] typically considered two types of experiments, i.e., those under CO_2-bearing and CO_2-free conditions. These contrasting conditions not only reflect geological records (such as strongly carbonated komatiites and carbonate-free, serpentinized komatiites) [69], but also the two types of fluid circulation paths. The first type addresses the direct reactions with Hadean–Archean seawater containing high concentration of ΣCO_2 [50]; this is similar to sulfate in modern seawater introduced directly through faults into reaction zones at the base of seafloor hydrothermal systems, forming sulfate minerals that strongly affect the redox state of hydrothermal fluid, e.g., [70,71].

The second type assumes reactions between komatiite and CO_2-free fluid in a reaction zone where CO_2 in downwelling seawater has been mostly precipitated as carbonate minerals in the surrounding rocks (e.g., recharge zone) before the fluid reaches reaction zones [49]. Previous studies revealed that the formation of carbonate minerals in the reaction zone suppressed H_2 generation given that most of iron originally contained in igneous phases was incorporated directly into carbonate minerals as Fe(II) without going through oxidation and reduction processes in water that generate H_2 [50]. The experiments in this study were a simulation of the CO_2-free hydrothermal alteration of komatiite in a reaction zone, which has higher reduction abilities than those in CO_2-bearing systems.

In this case, a certain amount of H_2 generation in the fluids was expected in the CO_2-free experiments. However, the H_2 concentrations in fluid in N350 is 1.7 mmol/kg, which is almost identical to or lower than that in CO_2-bearing experiments at 350 °C. On the contrary, the H_2 concentration in N250 is 100 times higher than that of the CO_2-bearing experiments at 250 °C (Table 3). This indicates that the reduction ability of komatiite was partially used for the reduction of nitrate during the experiments, as discussed in Section 4.2. Accordingly, the potential H_2 concentrations were calculated for the case where

nitrate was not included in the initial solutions to assess the maximum H_2 generation ability of komatiite during its alteration at 250 °C and 350 °C. Using the $N_2(aq)/NH_3(aq)$ ratio of 4.5 in experiments N250 and N350, the presumed mass balance reaction of nitrate reduction by $H_2(aq)$ that is generated from the reaction of ferrous iron with water can be expressed as

$$20NO_3^- + 20H^+ + 53H_{2(aq)} = 9N_{2(aq)} + 2NH_{3(aq)} + 60H_2O. \quad (25)$$

This reaction implies that the reduction of nitrate in the initial fluid requires 2.6 times $H_{2(aq)}$, suggesting that an additional 26 mmol/kg and 2.6 mmol/kg of $H_{2(aq)}$ were potentially generated in N250 and N350, respectively. Certainly, these values should be upper limits for H_2 concentrations given than nitrate can be reduced by ferrous iron (Section 4.2.). However, the potential H_2 concentrations in N250 and N350 and the results of the previous CO_2-free experiment at 300 °C (H_2 = 23 mmol/kg) [49] suggests that the optimal temperature range for H_2 generation is 250–300 °C during the serpentinization of Al-depleted komatiite in CO_2-free conditions. This temperature range is comparable to the optimal temperature range for H_2 generation during the serpentinization of peridotites inferred from thermodynamic constraints [68,72].

4.4. Roles of Komatiite-Hosted Hydrothermal System on Pre-Biotic Chemistry

Komatiite-hosted hydrothermal systems have influenced pre-biotic chemistry and affected the sustainability of primitive microbial communities through the production of H_2, alkalinization of fluids, and ammonia production in the komatiite–H_2O–NO_3^- system.

H_2 is a key molecule for pre-biotic chemistry and energy metabolism. Theoretical predictions for the thermodynamic state of pre-biotic chemical evolution have highlighted that an H_2-rich hydrothermal environment was energetically advantageous for the synthesis and preservation of amino and fatty acids [73]. Further, the most plausible energy metabolisms to support the emergence and early evolution of life are considered to be H_2-driven hydrogenotrophic methanogenesis/acetogenesis and/or methanotrophic acetogenesis, e.g., [43,45,46]. On the basis of fluid chemistry and mineralogy in the komatiite–H_2O–CO_2 system, Ueda et al. (2016) have suggested that H_2-rich fluid might not have been produced by the hydrothermal alteration of komatiite under CO_2-bearing conditions at temperatures $\leq$ 250 °C [50]. This implies that hydrothermal systems on the deep seafloor (more than 1000 m below the sea surface) were favorable for the sustainability of primitive microbial communities as high hydrostatic pressure was necessary to create high-temperature fluids. In contrast, the steady-state H_2 concentrations in the komatiite–H_2O–NO_3^- system at 250 °C were 2.3 mmol/kg for experiment N250 and could be as high as 26 mmol/kg if the initial nitrate concentration is lower than 10 mmol/kg (Section 4.3). Such hydrogen concentrations are comparable to those in high-temperature hydrothermal fluids venting from a modern, peridotite-hosted system that harbors H_2-based chemosynthetic microbial communities, including methanogens (H_2 = 3–16 mmol/kg) (e.g., Kairei and Rainbow Fields) [74,75]. Thus, H_2-based, primitive microbial communities in the Hadean ocean may have developed in komatiite-hosted hydrothermal systems of lower fluid temperature (down to 250 °C) than previously thought.

Alkaline fluids were necessary for primordial metabolisms driven by chemiosmosis and electrochemistry at the vent–ocean interface (i.e., hydrothermal mounds), where hydrothermal fluids mixed with acidic and/or neutral, CO_2-rich Hadean seawater [76–78]. For example, the selective synthesis of alanine from pyruvate and ammonia (>30% in yield) occurs in water with pH of 9–11 at 70 °C in the presence of iron oxyhydroxides [76]. Certain steps in the reductive tricarboxylic acid cycle are promoted by FeS-Fe_0 assemblages that can be produced electrochemically in alkaline water with pH of 10 at 100 °C in the presence of 1 mmol/kg H_2 [78]. This study shows that the pH of fluid in the komatiite–H_2O–NO_3^- system becomes more alkaline than that in the komatiite–H_2O–CO_2 system at 250 °C ($pH_{25°C}$ = 8.7 and 6.0, respectively) (Table 3). Thus, hydrothermal fluids generated in the komatiite–H_2O–NO_3^- system may have been more favorable to certain types of primordial metabolisms at the vent–ocean interface where the reaction zone temperature

was around 250 °C. In contrast, when the temperature of the reaction zone rises over 350 °C, the hydrothermal fluids in the komatiite–H_2O–CO_2 system become more favorable for primordial metabolisms as the destabilization of carbonate minerals above 350 °C stimulates the alkalinization effect by ΣCO_2 in the aqueous fluid, producing an alkaline pH in the CO_2-bearing fluid [48,50,79].

Ammonia is produced from nitrate at a high yield (10%) in the komatiite–H_2O–NO_3^- system both at 250 °C and 350 °C (Table 1). Ammonia is a key reactant for synthesizing amino and nucleic acids, and previous research successfully produced organic nitrogen compounds (amides, amino acids, and nitriles) by reacting ammonia with a variety of organic compounds (e.g., methane, formic acid, oxalic acid, and pyruvate) under limited hydrothermal conditions with and without minerals [76,80–83]. As the fluid residence time from the onset of the high-temperature (>200 °C) reaction to venting at the seafloor (several years for present-day hydrothermal systems) [84,85] is much longer than the time required for complete reduction of nitrate at ≥250 °C (<300 h) (Table 1), a stable supply of ammonia to hydrothermal environments could be expected for the komatiite–H_2O–NO_3^- system in the Hadean ocean. Although the actual concentration of nitrate in the early oceans (thus, ammonia concentration in hydrothermal fluids) may have been lower than that used in our experiments, the stable supply of ammonia may have allowed abiotic synthesis of organic nitrogen compounds at least in localized environments that can concentrate ammonia such as pore spaces of clay mineral clusters in altered komatiite crusts, and interiors of iron oxyhydroxides in hydrothermal mounds (e.g., Figure 5g). However, further studies are necessary to explore pathways for the synthesis of organic nitrogen compounds that are resistant to the fluctuation of environmental conditions (pH, temperature and coexisting mineral type) that the hydrothermal vent environments probably encountered.

4.5. Implications for Biological Nitrogen Metabolism, Phytosynthetic Activity, and the Global Nitrogen Cycle in the Early Earth

The stable and high-yield production of ammonia in the komatiite–H_2O–NO_3^- system is an important process not only for pre-biotic chemistry in the hydrothermal environments but also for controlling ammonia concentrations in the early global ocean that probably influenced biological nitrogen metabolism, the development of photosynthetic ecosystems, and global nitrogen cycle in the early Earth. Approximations of the ammonia production rate in the komatiite-hosted hydrothermal systems in the early ocean, $F_{NH3,ko}$ (mol/y), suggest that biological activity had started in hydrothermally influenced local environments, but was not likely widespread throughout the global surface ocean. The $F_{NH3,ko}$ (mol/y) value can be estimated from the following relation:

$$F_{NH3,ko} = Y_{NH3,ko}\, F_{H2O,ko}\, C_{NO3}, \quad (26)$$

where $Y_{NH3,ko}$ is the yield of ammonia by thermochemical nitrate reduction in the komatiite-hosted hydrothermal systems, F_{H2O} is the high-temperature (≥250 °C) fluid flux from the komatiite-hosted hydrothermal systems (kg/y), and C_{NO3} is the nitrate concentration in seawater (mol/kg). Our experiments suggest that $Y_{NH3,ko}$ value is 0.1, whereas numerical modeling by Laneuville et al. (2018) indicated that C_{NO3} in early seawater was dependent upon atmospheric nitrate production rate and had a range from 10^{-6} to 10^{-2} mol/kg [86], cf. [87,88]. The F_{H2O} value is initially approximated below, followed by the F_{NH3} value.

In the modern ocean, hydrothermal fluid flux is considered proportional to the annual production rate of oceanic crust at fast-spreading ridges [89]. Numerical modeling also suggests that plate velocity has not changed much throughout Earth's history [90,91]. Thus, the high-temperature fluid flux from the komatiite-hosted hydrothermal systems can be approximated as follows:

$$F_{H2O,ko} = k\, P_{ko}, \quad (27)$$

where P_{ko} is the annual komatiite production rate (km^3/y) and k is a coefficient that relates high-temperature fluid flux to P_{ko} (kg/km^3). Field observations suggest that the

thickness of the Archean oceanic crust was approximately three times greater than modern equivalents owing to the higher degree of partial melting [41,42]. Further, numerical modeling suggests that the global spreading rate of Archean oceanic crust (the product of plate velocity and plate boundary length: km^2/year) was approximately three times higher than that at present [90]. Thus, the annual production rate of Archean oceanic crust was estimated to be 180 km^3/y, that is, nine times greater than at present [92]. If the production ratio of oceanic plateau to oceanic crust at mid-oceanic ridges in the Archean was identical to that at present (0.05), the P_{ko} value was estimated to be 10 km^3/y in the Archean, which is nine times greater than that of the present oceanic plateau (1.1 km^3/year) [93]. Given that high-temperature (>250 °C) fluid flux in the modern ocean is estimated to be 0.2–3 × 10^{13} kg/y, e.g., [94–96], k is calculated to be 10^{11}–10^{12} kg/km^3. Collectively, the $F_{H2O,ko}$ and $F_{NH3,ko}$ values of the Archean ocean are estimated to be 10^{12}–10^{13} kg/y and 10^5–10^{10} mol/y, respectively (Table 8). Given higher heat flux from Earth's interior in the Hadean than Archean, the $F_{H2O,ko}$ and $F_{NH3,ko}$ values of the Hadean ocean are considered to be greater than the Archean ocean.

Table 8. Estimates of ammonia and dinitrogen production rates by thermochemical nitrate reduction in the early oceans.

Symbol	Units	Estimate (Hadean to Archaean Eon)
$Y_{NH3,ko}$		0.1
k	kg/km^3	10^{11}–10^{12}
P_{ko}	kg/km^3	10
$F_{H2O,ko}$	kg/y	10^{12}–10^{13}
C_{NO3}	mol/kg	10^{-6}–10^{-2}
$F_{NH3,ko}$	mol/y	10^5–10^{10}
$F_{N2,ko}$	mol/y	10^6–10^{11}
F_{N2}	mol/y	10^7–10^{12}

See text for the definition of symbol.

The $F_{NH3,ko}$ value provide insights into the evolution of biological nitrogen metabolism. It has to be noted that our estimate of the $F_{NH3,ko}$ value is based on simple equations and several assumptions, thus allowing the $F_{NH3,ko}$ value to have a wide range from 10^5 to 10^{10} mol/y. Nonetheless, our estimate indicates that the ammonia concentration in the early oceans had increased to 0.01–1000 μmol/kg from 4.4 Ga to 3.4 Ga if ammonia consumption rate in the ocean (e.g., biological assimilation) was much lower than the ammonia production rate. Microorganism can assimilate ammonia at the micro-to-milli molal levels for growth. For example, a half saturation constant for ammonia uptake has been reported to be 4–74 μmol/kg for bacteria isolated from different habitats [97]. Thus, if nitrate concentration in the early oceans was greater than 10 μmol/kg, the long-term production of ammonia through thermochemical nitrate reduction for the first billion years might have allowed the subsequent development of an early biosphere in the global surface ocean. In contrast, if nitrate concentration in the early oceans was less than 1 μmol/kg, komatiite-hosted hydrothermal activity would not have contributed to the accumulation of ammonia in the global ocean. In this case, the onset of biological nitrogen fixation ($N_2 \rightarrow NH_3$) was required for the development of early biosphere, consistent with genomic, physiologic, and geological records that are compatible with nitrogen fixation by the last universal common ancestor or methanogen in hydrothermal environments at 3.5 Ga [4,5,98,99], cf. [100]. To determine which scenario is more appropriate for the evolutional history of nitrogen metabolism, future work is required to estimate nitrate concentration in early seawater from geological records. Nitrogen isotopic characterization of abiotically produced ammonia is also important to determine the source of nitrogen isotopic compositions in Archean sedimentary rocks of marine origin, which have been interpreted as evidence for biological nitrogen fixation in surface oceans at 3.2 Ga [101] on the basis of nitrogen isotopic similarity to N_2 in the Archean atmosphere (ca. 0‰) [10,102–104].

Results of our experiments also suggest that 90% of nitrate nitrogen introduced to the komatiite-hosted hydrothermal system had probably been converted to N_2, resulting in a larger input of N_2 to the early ocean than that of ammonia. The higher input of N_2 may have stabilized the partial pressure of N_2 (pN_2) in the atmosphere and climate in an era of low solar luminosity as the increase in pN_2 would have increased the warming effect of existing greenhouse gases in an anoxic atmosphere (CO_2, CH_4) [105]. The approximate global N_2 flux from thermochemical nitrate reduction in early Archean seafloor hydrothermal systems, including both komatiite- and basalt-hosted systems, is F_{N2} (mol/y), which can be compared to the N_2 fluxes from other processes to develop a quantitative assessment of the contribution of thermochemical nitrate reduction to pN_2 in the early Archean.

The estimated F_{N2} value in the early Archean includes the estimate of the N_2 production rate in the komatiite-hosted hydrothermal system in the early Archean, $F_{N2,ko}$ (mol/y) using the following equation:

$$F_{N2,ko} = Y_{N2,ko}\, F_{H2O,ko}\, C_{NO3}, \quad (28)$$

where $Y_{N2,ko}$ is the yield of N_2 by thermochemical nitrate reduction in the komatiite-hosted hydrothermal systems. By substituting 0.45, 10^{12}–10^{13} kg/y, and 10^{-6}–10^{-2} mol/kg for $Y_{N2,ko}$, $F_{H2O,ko}$, and C_{NO3} in Equation (28), respectively, $F_{N2,ko}$ is calculated to be 10^{6}–10^{11} mol/y. If the production ratio of oceanic plateau to oceanic crust at mid-oceanic ridges in the Archean was identical to that at present (0.05), high-temperature fluid flux from the basalt-hosted hydrothermal system at Archean mid-oceanic ridges is one order magnitude larger than $F_{H2O,ko}$. Accordingly, F_{N2} is estimated to be 10^{7}–10^{12} mol/y (i.e., 10^{8}–10^{13} gN/y) in the early Archean, if the yield of N_2 by thermochemical nitrate reduction in the basalt-hosted system $Y_{N2,mo}$ had been equal or greater than $Y_{N2,ko}$, which is an appropriate assumption due to lower potentials of H_2 and NH_3 generation in basalt-hosted system than komatiite-hosted system.

When comparing N_2 fluxes from major processes, the F_{N2} value in the early Archean is quantitatively important. Major processes that supply N_2 to the present atmosphere are biological denitrification in the global ocean ($NO_3^- \rightarrow N_2$) ($1–3 \times 10^{14}$ gN/y) [106], degassing from the MORB source mantle (3×10^{10} gN/y) [107] and degassing by arc volcanism (3×10^{11} gN/y) [108]. In the early Archean, geological records suggest that biological denitrification was not yet underway, whereas degassing fluxes of N_2 from the MORB source mantle and via arc volcanism could have been one order of magnitude greater than today as they change proportionally with the annual production rate of oceanic crust. Therefore, N_2 flux by thermochemical nitrate reduction in the global hydrothermal systems would have been greater than that from the Earth's interior if nitrate concentration in Archean seawater had been greater than 1000 μmol/kg.

In summary, the approximate N_2 fluxes to the atmosphere in the early Archean from hydrothermal systems by thermochemical nitrate reduction and from the Earth's interior were 10^{8}–10^{13} gN/y and 10^{12} gN/y, respectively. Meanwhile, fluid inclusions in the Archean rock samples indicate that the abundance of N_2 in the Archean atmosphere was $2–12 \times 10^{21}$ gN, which is 0.5–3 times the present atmospheric N_2 [10,103,104,109]. Therefore, the residence time of atmospheric N_2 in the early Archean is calculated to be 10^{8} y or greater. For comparison, the residence time of atmospheric N_2 at present is 10^{7} years due to the high rates of biological nitrogen fixation and biological denitrification in the global ocean ($1–3 \times 10^{14}$ gN/y) [106]. Although pN_2 and its secular variation during Earth history have not yet been estimated precisely, our simple estimate implies that pN_2 is stable for $\geq 10^{8}$ years in the early Archean if the global nitrogen cycle was driven primarily by abiotic nitrogen processes in the atmosphere and seafloor hydrothermal systems. Together with the emission of hydrogen and methane gases during serpentinization, this point should be considered when evaluating the role of hydrothermal activity in the long-term climate of the early Earth.

5. Conclusions

We conducted hydrothermal experiments simulating the high-temperature, high-pressure reactions between nitrate in seawater to find probable chemical pathways to deliver ammonia to the vent–ocean interface of komatiite-hosted hydrothermal systems and the global ocean on geological timescales. Our experiments provide the following key results and conclusions.

- In the komatiite–H_2O–NO_3^- system, ammonia was produced from nitrate with yields of 10% at 250 °C and 350 °C in a CO_2-free condition. The fluid chemistry and mineralogy suggest that nitrate reduction co-occurred with serpentinization and andradite formation at 250 °C, whereas it co-occurred with serpentinization at 350 °C. This represents a case where CO_2 in downwelling fluid precipitated as carbonate minerals in surrounding rocks before reaching the high-temperature reaction zones.
- Nitrate reduction by both H_2 and Fe^{III} at the site of serpentinization and andradite formation probably contributed to a lower $N_{2(aq)}/NH_{3(aq)}$ ratio (4.5) than expected due to the thermodynamic equilibrium of dissolved nitrogen species in N–H–O system at 250 °C and 350 °C, 500 bars.
- H_2-rich and alkaline fluids, which are prerequisites for both prebiotic and primordial metabolisms, were generated in the komatiite–H_2O–NO_3^- system at lower temperatures (down to 250 °C) than previously thought under CO_2-rich conditions. The komatiite–H_2O–NO_3^- system also provided a stable supply of ammonia to the hydrothermal environments for biomolecule synthesis. Given that the temperature of hydrothermal fluids depends on hydrostatic pressure, the komatiite–H_2O–NO_3^- system probably reduces the minimum water depth of seafloor hydro-thermal systems to about 1000 m, which may have favored the start of pre-biotic chemistry and the sustainable development of H_2-based microbial ecosystems at the vent-ocean interface of the Hadean ocean.
- The ammonia production rate in the komatiite-hosted hydrothermal systems depends on nitrate concentration in seawater and is estimated to be 10^5–10^{10} mol/y in the Archean ocean. The rate in the Hadean ocean was likely to be greater than the Archean ocean given higher heat flux in the Hadean ocean. If nitrate concentrations in the early oceans were greater than 10 μmol/kg, the long-term production of ammonia by thermochemical nitrate reduction for the first billion years might have allowed the subsequent development of an early biosphere in the global surface ocean through biological ammonia assimilation.
- The N_2 production rate in the komatiite-hosted hydrothermal systems is estimated to be 10^6–10^{11} mol/y in the Archean ocean. The estimate implies that pN_2 in the Archean atmosphere is stable at least for 10^8 years if abiotic nitrogen processes in the atmosphere and seafloor hydrothermal systems mainly drove the global nitrogen cycle.

Collectively, these findings imply that komatiite-hosted systems might have impacted not only H_2-based chemosynthetic ecosystems at the vent-ocean interface but also photosynthetic ecosystems on the early Earth.

Author Contributions: Conceptualization, M.N., T.S. (Takazo Shibuya) and K.T.; experiments, M.N., A.M., T.S. (Takuya Saito) and M.S.; modeling, H.U. and T.S. (Takazo Shibuya); data curation, A.M.; writing—original draft preparation, M.N., H.U., T.S. (Takuya Saito) and T.S. (Takazo Shibuya); writing—review and editing, K.T.; project administration, M.N.; funding acquisition, M.N., M.S., T.S. (Takazo Shibuya) and K.T. All authors have read and agreed to the published version of the manuscript.

Funding: This research was funded by Grants-in-aid for Scientific Research from the Japan Society for Promotion of Science (KAKENHI JSPS), grant numbers JP15H03740, JP15H03741, JP17H06455, and JP17H01176, and the Mitsubishi Foundation, grant number 28120. The APC was funded by JP17H06454.

Institutional Review Board Statement: Not applicable.

Informed Consent Statement: Not applicable.

Data Availability Statement: The data presented in this study are available on request from the corresponding author.

Acknowledgments: The Authors thank M. Uematsu, T. Arai and T. Sato for their technical supports of SEM/EDS and XRF analyses.

Conflicts of Interest: The authors declare no conflict of interest.

Appendix A. Derivation of Reactions 19–24

Nitrate reduction to $N_{2(aq)}$ or $NH_{3(aq)}$ by $H_{2(aq)}$ is written as follows:

$$2NO_3^- + 2H^+ + 5H_{2(aq)} = N_{2(aq)} + 6H_2O, \quad \text{(A1)}$$

$$2NO_3^- + 2H^+ + 8H_{2(aq)} = 2NH_{3(aq)} + 6H_2O. \quad \text{(A2)}$$

Combining reactions A1 and A2 with reactions 1 and 2, reactions 19 to 24 are derived.

Appendix B. Operational Settings to Measure Mineralogical and Chemical Compositions of Solid Samples

- The accelerating voltages for the secondary electron imaging and semi-quantitative chemical analyses by SEM/EDX were 5 kV and 15 kV, respectively.
- EPMA parameters for the quantitative analyses were 15 kV of accelerating voltage, and 12 nA of specimen current.
- XRD analyses were conducted at 30 kV and 15 mA using Cu–Kα radiation. XRD peaks were assigned with the aid of PDXL software using the Inorganic Crystal Structure Database.
- XRF analyses were conducted at 50 kV and 60 mA using an Rh target.
- Raman spectra of the solid reaction products were obtained with 532 nm excitation. The incident laser power density was typically 100–700 kW/cm^2 for 100× (NA, 0.90) objective lenses. The final laser power at the sample surface was estimated to be 1–3 mW, and the spatial resolution of the Raman analysis was finer than 1 μm. Each point typically was scanned three times for 10–90 s from 100 to 2600 cm^{-1} at a spectral resolution of 2.3 cm^{-1} with a grating containing 600 grooves/mm. The Raman shift was calibrated using a silicon wafer prior to the analyses.

Appendix C

Table A1. Abbreviations and compositions used in this study.

Act = Actinolite, $Ca_2(Mg,Fe)_5Si_8O_{22}(OH)_2$
Ad = Andradite, $Ca_3Fe^{III}{}_2Si_3O_{12}$
Aug = Augite, $(Ca,Mg,Fe)_2Si_2O_6$
Chl = Chlorite
Chry = Chrysotile, $Mg_3Si_2O_5(OH)_4$
Clin = Clinochlore, $(Mg_5Al)(Si_3Al)O_{10}(OH)_8$
Cpx = Clinopyroxene
Diop = Diopside, $CaMgSi_2O_6$
For = Forsterite, Mg_2SiO_4
Faya = Fayalite, Fe_2SiO_4
Hal = Halite, NaCl
Mgt = Magnetite, Fe_3O_4
Ol = Olivine, $(Mg,Fe)_2SiO_4$
Sap = Saponite, $Ca_{0.25}(Mg_{2.5}Fe_{0.5})\ (Si_{3.5}Al_{0.5})O_{10}(OH)_2{\cdot}4H_2O$
Sme = Smectite
SiO_2 (am) = Amorphous silica, SiO_2
Srp = Serpentine, $(Mg,Fe)_3Si_2O_5(OH)_4$
Vrm = Vermiculite, $(Mg,Fe^{II},Al)_3(Si,Al)_4O_{10}(OH)_2{\cdot}4H_2O$
Wol = Wollastonite, $CaSiO_3$

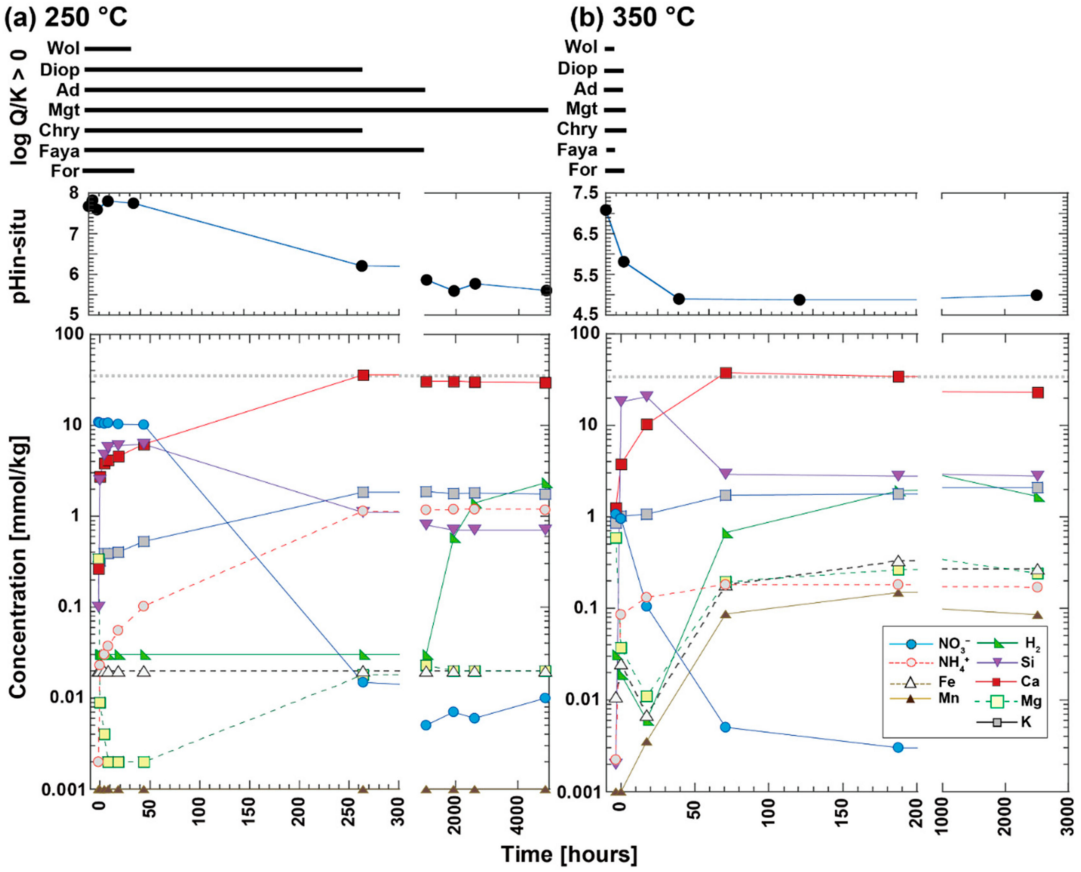

Figure A1. Time trends for saturation index, $pH_{in\text{-}situ}$, and dissolved species concentrations of fluids from experiments in the komatiite–H_2O–NO_3^- system at 250 °C (**a**) and 350 °C (**b**).

References

1. Orgel, L.E. Prebiotic Chemistry and the Origin of the RNA World. *Crit. Rev. Biochem. Mol. Biol.* **2004**, *39*, 99–123. [CrossRef]
2. Martin, W.; Russell, M.J. On the origin of biochemistry at an alkaline hydrothermal vent. *Philos. Trans. R. Soc. B Biol. Sci.* **2007**, *362*, 1887–1926. [CrossRef] [PubMed]
3. Navarro-Gonzãlez, R.; McKay, C.P.; Mvondo, D.N. A possible nitrogen crisis for Archaean life due to reduced nitrogen fixation by lightning. *Nature* **2001**, *412*, 61–64. [CrossRef]
4. Raymond, J.; Siefert, J.L.; Staples, C.R.; Blankenship, R.E. The Natural History of Nitrogen Fixation. *Mol. Biol. Evol.* **2004**, *21*, 541–554. [CrossRef]
5. Nishizawa, M.; Miyazaki, J.; Makabe, A.; Koba, K.; Takai, K. Physiological and isotopic characteristics of nitrogen fixation by hyperthermophilic methanogens: Key insights into nitrogen anabolism of the microbial communities in Archean hydrothermal systems. *Geochim. Cosmochim. Acta* **2014**, *138*, 117–135. [CrossRef]
6. Kasting, J.F.; Eggler, D.H.; Raeburn, S.P. Mantle redox evolution and the oxidation state of the Archean atmosphere. *J. Geol.* **1993**, *101*, 245–257. [CrossRef] [PubMed]
7. Rye, R.; Holland, H.D. Paleosols and the evolution of atmospheric oxygen: A critical review. *Am. J. Sci.* **1998**, *298*, 621–672. [CrossRef] [PubMed]
8. Kitajima, K.; Maruyama, S.; Utsunomiya, S.; Liou, J.G. Seafloor hydrothermal alteration at an Archaean mid-ocean ridge. *J. Metamorph. Geol.* **2001**, *19*, 583–599. [CrossRef]
9. Ohmoto, H.; Watanabe, Y.; Kumazawa, K. Evidence from massive siderite beds for a CO_2-rich atmosphere before, 1.8 billion years ago. *Nature* **2004**, *429*, 395–399. [CrossRef] [PubMed]
10. Nishizawa, M.; Sano, Y.; Ueno, Y.; Maruyama, S. Speciation and isotope ratios of nitrogen in fluid inclusions from seafloor hydrothermal deposits at similar to 3.5 Ga. *Earth Planet. Sci. Lett.* **2007**, *254*, 332–344. [CrossRef]
11. Shibuya, T.; Kitajima, K.; Komiya, T.; Terabayashi, M.; Maruyama, S. Middle Archean ocean ridge hydrothermal metamorphism and alteration recorded in the Cleaverville area, Pilbara Craton, Western Australia. *J. Metamorph. Geol.* **2007**, *25*, 751–767. [CrossRef]
12. Navarro-González, R.; Molina, M.J.; Molina, L.T. Nitrogen fixation by volcanic lightning in the early Earth. *Geophys. Res. Lett.* **1998**, *25*, 3123–3126. [CrossRef]

13. Summers, D.P.; Khare, B. Nitrogen fixation on early Mars and other terrestrial planets: Experimental demonstration of abiotic fixation reactions to nitrite and nitrate. *Astrobiology* **2007**, *7*, 333–341. [CrossRef] [PubMed]
14. Mojzsis, S.J.; Arrhenius, G.; Mckeegan, K.D.; Harrison, T.M.; Nutman, A.P.; Friend, C.R.L. Evidence for life on Earth before 3,800 million years ago. *Nature* **1996**, *384*, 55–59. [CrossRef] [PubMed]
15. Rosing, M.T. 13C-depleted carbon microparticles in >3700-Ma sea floor sedimentary rocks from West Greenland. *Science* **1999**, *283*, 674–676. [CrossRef] [PubMed]
16. Ueno, Y.; Yurimoto, H.; Yoshioka, H.; Komiya, T.; Maruyama, S. Ion microprobe analysis of graphite from ca. 3.8 Ga metasediments, Isua supracrustal belt, West Greenland: Relationship between metamorphism and carbon isotopic composition. *Geochim. Cosmochim. Acta* **2002**, *66*, 1257–1268. [CrossRef]
17. Nishizawa, M.; Takahata, N.; Terada, K.; Komiya, T.; Ueno, Y.; Sano, Y. Rare-earth element, lead, carbon, and nitrogen geochemistry of apatite-bearing metasediments from the similar to 3.8 Ga Isua supracrustal belt, West Greenland. *Int. Geol. Rev.* **2005**, *47*, 952–970. [CrossRef]
18. Ohtomo, Y.; Kakegawa, T.; Ishida, A.; Nagase, T.; Rosing, M.T. Evidence for biogenic graphite in early Archaean Isua metasedimentary rocks. *Nat. Geosci.* **2014**, *7*, 25–28. [CrossRef]
19. Dodd, M.S.; Papineau, D.; Grenne, T.; Slack, J.F.; Rittner, M.; Pirajno, F.; O'Neil, J.; Little, C.T.S. Evidence for early life in Earth's oldest hydrothermal vent precipitates. *Nature* **2017**, *543*, 60. [CrossRef] [PubMed]
20. Tashiro, T.; Ishida, A.; Hori, M.; Igisu, M.; Koike, M.; Méjean, P.; Takahata, N.; Sano, Y.; Komiya, T. Early trace of life from 3.95 Ga sedimentary rocks in Labrador, Canada. *Nature* **2017**, *549*, 516. [CrossRef] [PubMed]
21. Van Zuilen, M.A.; Leopand, A.; Arrhenius, G. Reassessing the evidence for the earliest traces of life. *Nature* **2002**, *418*, 627–630. [CrossRef]
22. Papineau, D.; De Gregorio, B.T.; Cody, G.D.; Fries, M.D.; Mojzsis, S.J.; Steele, A.; Stroud, R.M.; Fogel, M.L. Ancient graphite in the Eoarchean quartz–pyroxene rocks from Akilia in southern West Greenland I: Petrographic and spectroscopic characterization. *Geochim. Cosmochim. Acta* **2010**, *74*, 5862–5883. [CrossRef]
23. Sano, Y.; Terada, K.; Takahashi, Y.; Nutman, A.P. Origin of life from apatite dating? *Nature* **1999**, *400*, 127–128. [CrossRef] [PubMed]
24. Buresh, R.J.; Moraghan, J.T. Chemical Reduction of Nitrate by Ferrous Iron. *J. Environ. Qual.* **1976**, *5*, 320–325. [CrossRef]
25. Summers, D.P.; Chang, S. Prebiotic ammonia from reduction of nitrite by iron (II) on the early Earth. *Nature* **1993**, *365*, 630–633. [CrossRef]
26. Hansen, H.C.B.; Koch, C.B.; Nancke-Krogh, H.; Borggaard, O.K.; Sørensen, J. Abiotic Nitrate Reduction to Ammonium: Key Role of Green Rust. *Environ. Sci. Technol.* **1996**, *30*, 2053–2056. [CrossRef]
27. Hansen, H.C.B. Reduction of nitrate to ammonium by sulphate green rust; activation energy and reaction mechanism. *Clay Miner.* **1998**, *33*, 87–101. [CrossRef]
28. Habicht, K.S. Calibration of Sulfate Levels in the Archean Ocean. *Science* **2002**, *298*, 2372–2374. [CrossRef]
29. Crowe, S.A.; Paris, G.; Katsev, S.; Jones, C.; Kim, S.-T.; Zerkle, A.L.; Nomosatryo, S.; Fowle, D.A.; Adkins, J.F.; Sessions, A.L.; et al. Sulfate was a trace constituent of Archean seawater. *Science* **2014**, *346*, 735–739. [CrossRef] [PubMed]
30. Zhelezinskaia, I.; Kaufman, A.J.; Farquhar, J.; Cliff, J. Large sulfur isotope fractionations associated with Neoarchean microbial sulfate reduction. *Science* **2014**, *346*, 742–744. [CrossRef]
31. Summers, D.P. Ammonia Formation By The Reduction Of Nitrite/Nitrate By Fes: Ammonia Formation Under Acidic Conditions. *Orig. Life Evol. Biosph.* **2005**, *35*, 299–312. [CrossRef] [PubMed]
32. Brandes, J.A.; Hazen, R.M.; Yoder, H.S., Jr. Inorganic nitrogen reduction and stability under simulated hydrothermal conditions. *Astrobiology* **2008**, *8*, 1113–1126. [CrossRef] [PubMed]
33. Smirnov, A.; Hausner, D.; Laffers, R.; Strongin, D.R.; Schoonen, M.A. Abiotic ammonium formation in the presence of Ni-Fe metals and alloys and its implications for the Hadean nitrogen cycle. *Geochem. Trans.* **2008**, *9*, 5. [CrossRef] [PubMed]
34. Singireddy, S.; Gordon, A.D.; Smirnov, A.; Vance, M.A.; Schoonen, M.A.; Szilagyi, R.K.; Strongin, D.R. Reduction of nitrite and nitrate to ammonium on pyrite. *Orig. Life Evol. Biosph.* **2012**, *42*, 275–294. [CrossRef]
35. Li, Y.; Yamaguchi, A.; Yamamoto, M.; Takai, K.; Nakamura, R. Molybdenum Sulfide: A Bioinspired Electrocatalyst for Dissimilatory Ammonia Synthesis with Geoelectrical Current. *J. Phys. Chem. C* **2017**, *121*, 2154–2164. [CrossRef]
36. German, C.R.; Von Damm, K.L. Hydrothermal processes. In *The Treatise on Geochemistry*; Turekian, K.K., Holland, H.D., Eds.; Elsevier: New York, NY, USA, 2004; Chapter 6.07; pp. 181–222.
37. Bourbonnais, A.; Lehmann, M.F.; Butterfield, D.A.; Juniper, S.K. Subseafloor nitrogen transformations in diffuse hydrothermal vent fluids of the Juan de Fuca Ridge evidenced by the isotopic composition of nitrate and ammonium. *Geochem. Geophys. Geosystems* **2012**, *13*, Q02T01. [CrossRef]
38. Nishizawa, M.; Koba, K.; Makabe, A.; Yoshida, N.; Kaneko, M.; Hirao, S.; Ishibashi, J.-i.; Yamanaka, T.; Shibuya, T.; Kikuchi, T.; et al. Nitrification-driven forms of nitrogen metabolism in microbial mat communities thriving along an ammonium-enriched subsurface geothermal stream. *Geochim. Cosmochim. Acta* **2013**, *113*, 152–173. [CrossRef]
39. Takahashi, E.; Scarfe, C.M. Melting of peridotite to 14 GPa and the genesis of komatiite. *Nature* **1985**, *315*, 566–568. [CrossRef]
40. Arndt, N.T.; Lesher, C.M.; Barnes, S.J. *Komatiite*; Cambridge University Press: Cambridge, UK, 2008.
41. Ohta, H.; Maruyama, S.; Takahashi, E.; Watanabe, Y.; Kato, Y. Field occurrence, geochemistry and petrogenesis of the Archean Mid-Oceanic Ridge Basalts (AMORBs) of the Cleaverville area, Pilbara Craton, Western Australia. *Lithos* **1996**, *37*, 199–221. [CrossRef]

42. Komiya, T. Material circulation model including chemical differentiation within the mantle and secular variation of temperature and composition of the mantle. *Phys. Earth Planet. Inter.* **2004**, *146*, 333–367. [CrossRef]
43. Takai, K.; Nakamura, K.; Suzuki, K.; Inagaki, F.; Nealson, K.; Kumagai, H. Ultramafics-Hydrothermalism-Hydrogenesis-HyperSLiME (UltraH^3) linkage: A key insight into early microbial ecosystem in the Archean deep-sea hydrothermal systems. *Paleontol. Res.* **2006**, *10*, 269–282. [CrossRef]
44. Russell, M.J.; Hall, A.J. The emergence of life from iron monosulphide bubbles at a submarine hydrothermal redox and pH front. *J. Geol. Soc.* **1997**, *154*, 377–402. [CrossRef] [PubMed]
45. Martin, W.; Baross, J.; Kelley, D.; Russell, M.J. Hydrothermal vents and the origin of life. *Nat. Rev. Microbiol.* **2008**, *6*, 805–814. [CrossRef] [PubMed]
46. Russell, M.J.; Barge, L.M.; Bhartia, R.; Bocanegra, D.; Bracher, P.J.; Branscomb, E.; Kidd, R.; McGlynn, S.; Meier, D.H.; Nitschke, W.; et al. The drive to life on wet and icy worlds. *Astrobiology* **2014**, *14*, 308–343. [CrossRef] [PubMed]
47. Yoshizaki, M.; Shibuya, T.; Suzuki, K.; Shimizu, K.; Nakamura, K.; Takai, K.E.N.; Omori, S.; Maruyama, S. H_2 generation by experimental hydrothermal alteration of komatiitic glass at 300°C and 500 bars: A preliminary result from on-going experiment. *Geochem. J.* **2009**, *43*, e17–e22. [CrossRef]
48. Shibuya, T.; Yoshizaki, M.; Masaki, Y.; Suzuki, K.; Takai, K.; Russell, M.J. Reactions between basalt and CO_2-rich seawater at 250 and 350°C, 500bars: Implications for the CO_2 sequestration into the modern oceanic crust and the composition of hydrothermal vent fluid in the CO_2-rich early ocean. *Chem. Geol.* **2013**, *359*, 1–9. [CrossRef]
49. Shibuya, T.; Yoshizaki, M.; Sato, M.; Shimizu, K.; Nakamura, K.; Omori, S.; Suzuki, K.; Takai, K.; Tsunakawa, H.; Maruyama, S. Hydrogen-rich hydrothermal environments in the Hadean ocean inferred from serpentinization of komatiites at 300 °C and 500 bar. *Prog. Earth Planet. Sci.* **2015**, *2*, 1–11. [CrossRef]
50. Ueda, H.; Shibuya, T.; Sawaki, Y.; Saitoh, M.; Takai, K.; Maruyama, S. Reactions between komatiite and CO_2-rich seawater at 250 and 350 °C, 500 bars: Implications for hydrogen generation in the Hadean seafloor hydrothermal system. *Prog. Earth Planet. Sci.* **2016**, *3*, 1–14. [CrossRef]
51. Nishizawa, M.; Sakai, S.; Konno, U.; Nakahara, N.; Takaki, Y.; Saito, Y.; Imachi, H.; Tasumi, E.; Makabe, A.; Koba, K.; et al. Nitrogen and Oxygen Isotope Effects of Ammonia Oxidation by Thermophilic Thaumarchaeota from a Geothermal Water Stream. *Appl. Environ. Microbiol.* **2016**, *82*, 4492–4504. [CrossRef] [PubMed]
52. Nishizawa, M.; Saitoh, M.; Matsui, Y.; Usui, Y.; Shibuya, T. Removal of organic contaminants from iron sulfides as a pretreatment for mineral-mediated chemical synthesis under prebiotic hydrothermal conditions. *Geochem. J.* **2017**, *51*, 495–505. [CrossRef]
53. Seyfried, W.E., Jr.; Janecky, D.R.; Berndt, M.E. Rocking autoclaves for hydrothermal experiments II. The flexible reaction-cell system. In *Hydrothermal Experimental Techniques*; Ulmer, G.C., Barns, H.L., Eds.; John Wiley and Sons: Hoboken, NJ, USA, 1987; pp. 216–239.
54. Wetzel, L.R.; Shock, E.L. Distinguishing ultramafic-from basalt-hosted submarine hydrothermal systems by comparing calculated vent fluid compositions. *J. Geophys. Res. Solid Earth* **2000**, *105*, 8319–8340. [CrossRef]
55. Bethke, C.M. *Geochemical and Biogeochemical Reaction Modeling*, 2nd ed.; Cambridge University Press: Cambridge, UK, 2008.
56. Johnson, J.W.; Oelkers, E.H.; Helgeson, H.C. SUPCRT92: A software package for calculating the standard molal thermodynamic properties of minerals, gases, aqueous species, and reactions from 1 to 5000 bar and 0 to 1000 °C. *Comput. Geosci.* **1992**, *18*, 899–947. [CrossRef]
57. Shock, E.L.; Helgeson, H.C.; Sverjensky, D.A. Calculation of the thermodynamic and transport properties of aqueous species at high pressures and temperatures: Standard partial molal properties of inorganic neutral species. *Geochim. Cosmochim. Acta* **1989**, *53*, 2157–2183. [CrossRef]
58. Shock, E.L.; Sassani, D.C.; Willis, M.; Sverjensky, D.A. Inorganic species in geologic fluids: Correlations among standard molal thermodynamic properties of aqueous ions and hydroxide complexes. *Geochim. Cosmochim. Acta* **1997**, *61*, 907–950. [CrossRef]
59. Shock, E.L.; Koretsky, C.M. Metal-organic complexes in geochemical processes: Estimation of standard partial molal thermodynamic properties of aqueous complexes between metal cations and monovalent organic acid ligands at high pressures and temperatures. *Geochim. Cosmochim. Acta* **1995**, *59*, 1497–1532. [CrossRef]
60. Sverjensky, D.A.; Shock, E.L.; Helgeson, H.C. Prediction of the thermodynamic properties of aqueous metal complexes to 1000°C and 5 kb. *Geochim. Cosmochim. Acta* **1997**, *61*, 1359–1412. [CrossRef]
61. Helgeson, H.C. Thermodynamics of hydrothermal systems at elevated temperatures and pressures. *Am. J. Sci.* **1969**, *267*, 729–804. [CrossRef]
62. Helgeson, H.C.; Kirkham, D.H. Theoretical prediction of the thermodynamic behavior of aqueous electrolytes at high pressures and temperatures; II, Debye-Huckel parameters for activity coefficients and relative partial molal properties. *Am. J. Sci.* **1974**, *274*, 1199–1261. [CrossRef]
63. Buatier, M.D.; Früh-Green, G.L.; Karpoff, A.M. Mechanisms of Mg-phyllosilicate formation in a hydrothermal system at a sedimented ridge (Middle Valley, Juan de Fuca). *Contrib. Mineral. Petrol.* **1995**, *122*, 134–151. [CrossRef]
64. Berger, A.; Gier, S.; Krois, P. Porosity-preserving chlorite cements in shallow-marine volcaniclastic sandstones: Evidence from Cretaceous sandstones of the Sawan gas field, Pakistan. *AAPG Bull.* **2009**, *93*, 595–615. [CrossRef]
65. Haile, B.G.; Hellevang, H.; Aagaard, P.; Jahren, J. Experimental nucleation and growth of smectite and chlorite coatings on clean feldspar and quartz grain surfaces. *Mar. Pet. Geol.* **2015**, *68*, 664–674. [CrossRef]

66. McCollom, T.M.; Klein, F.; Robbins, M.; Moskowitz, B.; Berquó, T.S.; Jöns, N.; Bach, W.; Templeton, A. Temperature trends for reaction rates, hydrogen generation, and partitioning of iron during experimental serpentinization of olivine. *Geochim. Cosmochim. Acta* **2016**, *181*, 175–200. [CrossRef]
67. Seyfried, W.E.; Mottl, M.J. Hydrothermal alteration of basalt by seawater under seawater-dominated conditions. *Geochim. Cosmochim. Acta* **1982**, *46*, 985–1002. [CrossRef]
68. Klein, F.; Bach, W.; Jöns, N.; Mccollom, T.; Moskowitz, B.; Berquó, T. Iron partitioning and hydrogen generation during serpentinization of abyssal peridotites from 15°N on the Mid-Atlantic Ridge. *Geochim. Cosmochim. Acta* **2009**, *73*, 6868–6893. [CrossRef]
69. Stiegler, M.T.; Lowe, D.R.; Byerly, G.R. The Petrogenesis of Volcaniclastic Komatiites in the Barberton Greenstone Belt, South Africa: A Textural and Geochemical Study. *J. Petrol.* **2010**, *51*, 947–972. [CrossRef]
70. Alt, J.C. Subseafloor processes in Mid-ocean ridge hydrothermal systems. In *Seafloor Hydrothermal Systems: Physical, Chemical, Biological and Geological Interactions*; Humphiris, S.E., Zierenberg, R.A., Mullineaux, L.S., Thomson, R.E., Eds.; Geophysical Monograph; Wiley & Sons: New York, NY, USA, 1995; Volume 91, pp. 85–114.
71. Butterfield, D.A.; Seyfried, W.E.; Lilley, M.D. Composition and evolution of hydrothermal fluids. In *Energy and Mass Transfer in Marine Hydrothermal Systems*; Halbach, P.E., Tunnicliffe, V., Hein, J.R., Eds.; Dahlem University Press: Berlin, Germany, 2003.
72. Mccollom, T.M.; Bach, W. Thermodynamic constraints on hydrogen generation during serpentinization of ultramafic rocks. *Geochim. Cosmochim. Acta* **2009**, *73*, 856–875. [CrossRef]
73. Amend, J.P.; McCollom, T.M. Energetics of Biomolecule Synthesis on Early Earth. In *Chemical Evolution II: From the Origins of Life to Modern Society*; American Chemical Society: Washington, DC, USA, 2009; Volume 1025, pp. 63–94.
74. Takai, K.; Gamo, T.; Tsunogai, U.; Nakayama, N.; Hirayama, H.; Nealson, K.H.; Horikoshi, K. Geochemical and microbiological evidence for a hydrogen-based, hyperthermophilic subsurface lithoautotrophic microbial ecosystem (HyperSLiME) beneath an active deep-sea hydrothermal field. *Extremophiles* **2004**, *8*, 269–282. [CrossRef] [PubMed]
75. Flores, G.E.; Campbell, J.H.; Kirshtein, J.D.; Meneghin, J.; Podar, M.; Steinberg, J.I.; Seewald, J.S.; Tivey, M.K.; Voytek, M.A.; Yang, Z.K.; et al. Microbial community structure of hydrothermal deposits from geochemically different vent fields along the Mid-Atlantic Ridge. *Environ. Microbiol.* **2011**, *13*, 2158–2171. [CrossRef] [PubMed]
76. Barge, L.M.; Flores, E.; Baum, M.M.; VanderVelde, D.G.; Russell, M.J. Redox and pH gradients drive amino acid synthesis in iron oxyhydroxide mineral systems. *Proc. Natl. Acad. Sci. USA* **2019**, *116*, 4828–4833. [CrossRef]
77. Kitadai, N.; Nakamura, R.; Yamamoto, M.; Takai, K.; Li, Y.; Yamaguchi, A.; Gilbert, A.; Ueno, Y.; Yoshida, N.; Oono, Y. Geoelectrochemical CO production: Implications for the autotrophic origin of life. *Sci. Adv.* **2018**, *4*, eaao7265. [CrossRef] [PubMed]
78. Kitadai, N.; Nakamura, R.; Yamamoto, M.; Takai, K.; Yoshida, N.; Oono, Y. Metals likely promoted protometabolism in early ocean alkaline hydrothermal systems. *Sci. Adv.* **2019**, *5*, eaav7848. [CrossRef]
79. Shibuya, T.; Komiya, T.; Nakamura, K.; Takai, K.; Maruyama, S. Highly alkaline, high-temperature hydrothermal fluids in the early Archean ocean. *Precambrian Res.* **2010**, *182*, 230–238. [CrossRef]
80. Yanagawa, H.; Kobayashi, K. Chapter 8 An experimental approach to chemical evolution in submarine hydrothermal systems. *Orig. Life Evol. Biosph.* **1992**, *22*, 147–159. [CrossRef]
81. Marshall, W.L. Hydrothermal synthesis of amino acids. *Geochim. Cosmochim. Acta* **1994**, *58*, 2099–2106. [CrossRef]
82. Rushdi, A.I.; Simoneit, B.R.T. Lipid formation by aqueous Fischer-Tropsch-type synthesis over a temperature range of 100 to 400?C. *Orig. Life Evol. Biosph.* **2001**, *31*, 103–118. [CrossRef] [PubMed]
83. Novikov, Y.; Copley, S.D. Reactivity landscape of pyruvate under simulated hydrothermal vent conditions. *Proc. Natl. Acad. Sci. USA* **2013**, *110*, 13283–13288. [CrossRef] [PubMed]
84. Kadko, D.; Butterfield, D.A. The relationship of hydrothermal fluid composition and crustal residence time to maturity of vent fields on the Juan de Fuca Ridge. *Geochim. Cosmochim. Acta* **1998**, *62*, 1521–1533. [CrossRef]
85. Kadko, D.; Gronvold, K.; Butterfield, D. Application of radium isotopes to determine crustal residence times of hydrothermal fluids from two sites on the Reykjanes Peninsula, Iceland. *Geochim. Cosmochim. Acta* **2007**, *71*, 6019–6029. [CrossRef]
86. Laneuville, M.; Kameya, M.; Cleaves, H.J.I. Earth Without Life: A Systems Model of a Global Abiotic Nitrogen Cycle. *Astrobiology* **2018**, *18*, 897–914. [CrossRef] [PubMed]
87. Wong, M.L.; Charnay, B.D.; Gao, P.; Yung, Y.L.; Russell, M.J. Nitrogen Oxides in Early Earth's Atmosphere as Electron Acceptors for Life's Emergence. *Astrobiology* **2017**, *17*, 975–983. [CrossRef] [PubMed]
88. Ranjan, S.; Todd, Z.R.; Rimmer, P.B.; Sasselov, D.D.; Babbin, A.R. Nitrogen Oxide Concentrations in Natural Waters on Early Earth. *Geochem. Geophys. Geosystems* **2019**, *20*, 2021–2039. [CrossRef]
89. Kawada, Y.; Seama, N.; Okino, K. Review of Oceanic Crustal Structure and Seafloor Hydrothermal Circulation. *J. Geogr.* **2009**, *118*, 1037–1063. [CrossRef]
90. Abbott, D.; Menke, W. Length of the global plate boundary at 2.4 Ga. *Geology* **1990**, *18*, 58–61. [CrossRef]
91. Korenaga, J. Plate tectonics, flood basalts and the evolution of Earth's oceans. *Terra Nova* **2008**, *20*, 419–439. [CrossRef]
92. Peacock, S.A. Fluid Processes in Subduction Zones. *Science* **1990**, *248*, 329–337. [CrossRef] [PubMed]
93. Clift, P.D.; Vannucchi, P.; Morgan, J.P. Crustal redistribution, crust–mantle recycling and Phanerozoic evolution of the continental crust. *Earth Sci. Rev.* **2009**, *97*, 80–104. [CrossRef]
94. Elderfield, H.; Schults, A. Mid-ocean ridge hydrothermal fluxes and the chemical composition of the ocean. *Ann. Rev. Earth Planet. Sci* **1996**, *24*, 191–224. [CrossRef]

95. Chan, L.-H.; Alt, J.C.; Teagle, D.A.H. Lithium and lithium isotope profiles through the upper oceanic crust: A study of seawater–basalt exchange at ODP Sites 504B and 896A. *Earth Planet. Sci. Lett.* **2002**, *201*, 187–201. [CrossRef]
96. Nielsen, S.G.; Rehkämper, M.; Teagle, D.A.H.; Butterfield, D.A.; Alt, J.C.; Halliday, A.N. Hydrothermal fluid fluxes calculated from the isotopic mass balance of thallium in the ocean crust. *Earth Planet. Sci. Lett.* **2006**, *251*, 120–133. [CrossRef]
97. Reay, D.S.; Nedwell, D.B.; Priddle, J.; Ellis-Evans, J.C. Temperature dependence of inorganic nitrogen uptake: Reduced affinity for nitrate at suboptimal temperatures in both algae and bacteria. *Appl. Environ. Microbiol.* **1999**, *65*, 2577–2584. [CrossRef] [PubMed]
98. Ueno, Y.; Yoshioka, H.; Maruyama, S.; Isozaki, Y. Carbon isotopes and petrography of kerogens in ~3.5-Ga hydrothermal silica dikes in the North Pole area, Western Australia. *Geochim. Cosmochim. Acta* **2004**, *68*, 573–589. [CrossRef]
99. Weiss, M.C.; Sousa, F.L.; Mrnjavac, N.; Neukirchen, S.; Roettger, M.; Nelson-Sathi, S.; Martin, W.F. The physiology and habitat of the last universal common ancestor. *Nat. Microbiol.* **2016**, *1*, 16116. [CrossRef] [PubMed]
100. Boyd, E.S.; Hamilton, T.L.; Peters, J.W. An alternative path for the evolution of biological nitrogen fixation. *Front. Microbiol.* **2011**, *2*, 205. [CrossRef]
101. Stueken, E.E.; Buick, R.; Guy, B.M.; Koehler, M.C. Isotopic evidence for biological nitrogen fixation by molybdenum-nitrogenase from 3.2 Gyr. *Nature* **2015**, *520*, 666–669. [CrossRef] [PubMed]
102. Sano, Y.; Pillinger, C.T. Nitrogen isotopes and N_2/Ar ratios in chests: An attempt to measure time evolution of atmospheric $\delta^{15}N$ value. *Geochem. J.* **1990**, *24*, 315–325. [CrossRef]
103. Marty, B.; Zimmermann, L.; Pujol, M.; Burgess, R.; Philippot, P. Nitrogen isotopic composition and density of the Archean atmosphere. *Science* **2013**, *342*, 101–104. [CrossRef] [PubMed]
104. Avice, G.; Marty, B.; Burgess, R.; Hofmann, A.; Philippot, P.; Zahnle, K.; Zakharov, D. Evolution of atmospheric xenon and other noble gases inferred from Archean to Paleoproterozoic rocks. *Geochim. Cosmochim. Acta* **2018**, *232*, 82–100. [CrossRef]
105. Goldblatt, C.; Claire, M.W.; Lenton, T.M.; Matthews, A.J.; Watson, A.J.; Zahnle, K.J. Nitrogen-enhanced greenhouse warming on early Earth. *Nat. Geosci.* **2009**, *2*, 891–896. [CrossRef]
106. Brandes, J.A.; Devol, A.H. A global marine-fixed nitrogen isotopic budget: Implications for Holocene nitrogen cycling. *Glob. Biogeochem. Cycles* **2002**, *16*, 1120. [CrossRef]
107. Hilton, D.R.; Fischer, T.P.; Marty, B. Noble gases and volatile recycling at subduction zones. In *Noble Gases in Geochemistry and Cosmochemistry, Reviews in Mineralogy and Geochemistry*; Porcelli, D., Ballentine, C.J., Wieler, R., Eds.; Mineralogical Society of America: Washington, DC, USA, 2002; Volume 47, pp. 319–370.
108. Sano, Y.; Takahata, N.; Nishio, Y.; Fischer, T.P.; Williams, S.N. Volcanic flux of nitrogen from the Earth. *Chem. Geol.* **2001**, *171*, 263–271. [CrossRef]
109. Pinti, D.L.; Hashizume, K.; Matsuda, J.i. Nitrogen and argon signatures in 3.8 to 2.8 Ga metasediments: Clues on the chemical state of the archean ocean and the deep biosphere. *Geochim. Cosmochim. Acta* **2001**, *65*, 2301–2315. [CrossRef]